

样式定义: Reference: 缩进: 左侧: 0 厘米, 悬挂缩进: 2 字符, 首行缩进: -2 字符

# ~~Synergistic Use of Active and Passive Satellite Observations for Monitoring Urban Fossil Fuel CO<sub>2</sub> Emission~~ ~~Active and Passive Satellite Observations Coupled with Carbon-Nitrogen Synergy for Urban Fossil Fuel CO<sub>2</sub> Emissions Monitoring~~

Jinchun Yi <sup>#,1</sup>, Yiyang Huang <sup>#,1</sup>, Ge Han <sup>\*,1,3</sup>, Hongyuan Zhang <sup>2</sup>, Zhipeng Pei <sup>2</sup>, Haotian Luo <sup>1</sup>, Yichi Zhang <sup>1</sup>, Tianqi Shi <sup>6</sup>, Siwei Li <sup>1,3</sup>, Wei Gong <sup>4,5</sup>

<sup>1</sup>Hubei Key Laboratory of Quantitative Remote Sensing of Land and Atmosphere, School of Remote Sensing and Information Engineering, Wuhan University, Wuhan 430079, China.

<sup>2</sup>State Key Laboratory of Information Engineering in Surveying, Mapping and Remote Sensing, Wuhan University, Luoyu Road No.129, Wuhan 430079, China.

<sup>3</sup>Perception and Effectiveness Assessment for Carbon-neutrality Efforts, Engineering Research Center of Ministry of Education, Institute for Carbon Neutrality, Wuhan University, Wuhan, China.

<sup>4</sup>Electronic Information School, Wuhan University, Wuhan, China.

<sup>5</sup>Wuhan Institute of Quantum Technology, Wuhan, China.

<sup>6</sup>Laboratoire des Sciences du Climat et de l'Environnement, LSCE/IPSL, CEA-CNRS-UVSQ, Université Paris-Saclay, 91198 Gif-sur-Yvette, France.

*Correspondence to:* Ge Han (udhan@whu.edu.cn)

<sup>#</sup> These authors contributed equally to this work.

**Abstract.** Accurate estimation of fossil fuel CO<sub>2</sub> (ffCO<sub>2</sub>) emissions is essential for climate prediction and the development of mitigation policies. Top-down carbon – nitrogen joint observations offer the potential for more reliable ffCO<sub>2</sub> estimates. Here, we establish an inversion framework for urban ffCO<sub>2</sub> emissions based on combined active–passive satellite observations. Urban ffCO<sub>2</sub> distributions were first constructed using satellite NO<sub>2</sub> data and CO<sub>2</sub>-NO<sub>x</sub> emission ratios, and monthly ffCO<sub>2</sub> emissions for selected global cities were then estimated by integrating [the total column dry-air carbon dioxide \(XCO<sub>2</sub>\) observations](#) from the DQ-1 ACDL instrument. Our results show that satellite-derived NO<sub>x</sub> emissions provide strong constraints on urban anthropogenic CO<sub>2</sub> estimates. Validation against TCCON ground-based observations indicates that, compared with conventional top-down inversion approaches, our method more accurately reproduces urban ffXCO<sub>2</sub> plume distributions. We further evaluated the influence of different CO<sub>2</sub>-NO<sub>x</sub> ratio calculation methods on ffCO<sub>2</sub> estimates and found variations exceeding 150, exerting a substantial impact on emission inversions. Under observational constraints, the uncertainty in CO<sub>2</sub>-NO<sub>x</sub> ratios derived from different methods decreased by 9.79 – 38.78%, and the variation range was reduced by more than 100%, converging toward a consistent magnitude. This study advances understanding of the spatiotemporal patterns of urban ffCO<sub>2</sub> emissions and provides a unified perspective for future CO<sub>2</sub>-NO<sub>x</sub>-based anthropogenic carbon emission estimation.

## 1. Introduction

The intensification of global climate change has driven an increasing demand for high-precision monitoring of fossil fuel CO<sub>2</sub> (ffCO<sub>2</sub>) emissions (Agency, 2009). The Paris Agreement emphasizes that countries need rapid and timely access to changes in carbon emissions to support policy formulation and implementation. Achieving this goal relies on accurate and verifiable carbon accounting systems. Cities, due to their high concentration of population, energy consumption, and economic activity, contribute over 70% of global anthropogenic CO<sub>2</sub> emissions, making them key units for evaluating emission reduction policies and compliance monitoring (Crippa et al., 2018). Existing global and regional emission inventories primarily adopt bottom-up statistical accounting methods, estimating emissions based on energy production and sector-specific emission factors (Xu et al., 2024; Wei, 2024). However, these inventories often suffer from significant uncertainties due to data delays and incompleteness (Andres et al., 2012; Zhang et al., 2009; Le Quéré et al., 2018).

To overcome the limitations of bottom-up approaches, top-down atmospheric inversion techniques have advanced rapidly in recent years, enabling constraints on regional carbon budgets. Passive satellite remote sensing systems, such as GOSAT and OCO-2/3, can invert XCO<sub>2</sub> over large portions of the globe and have unique potential for identifying local point sources, estimating regional carbon fluxes, and inferring gross primary productivity (Schwandner et al., 2017; Eldering et al., 2017; Köhler et al., 2018; Han et al., 2018; Sun et al., 2018b). Nonetheless, top-down inversion methods also rely on accurate prior emission estimates. Inventories that downscale national or regional emissions to high spatial and temporal resolution often suffer from incomplete socio-economic data and inaccurate emission conversion factors, leading to substantial uncertainties in urban emission estimates (Gately and Hutyra, 2017). Moreover, conventional top-down CO<sub>2</sub> inversion studies have focused primarily on quantifying terrestrial ecosystem carbon fluxes, typically assuming fossil fuel emissions are known and unbiased. This complicates direct inference of anthropogenic emissions from CO<sub>2</sub> observations due to the atmospheric mixing of fossil fuel and ecosystem fluxes (Ye et al., 2020).

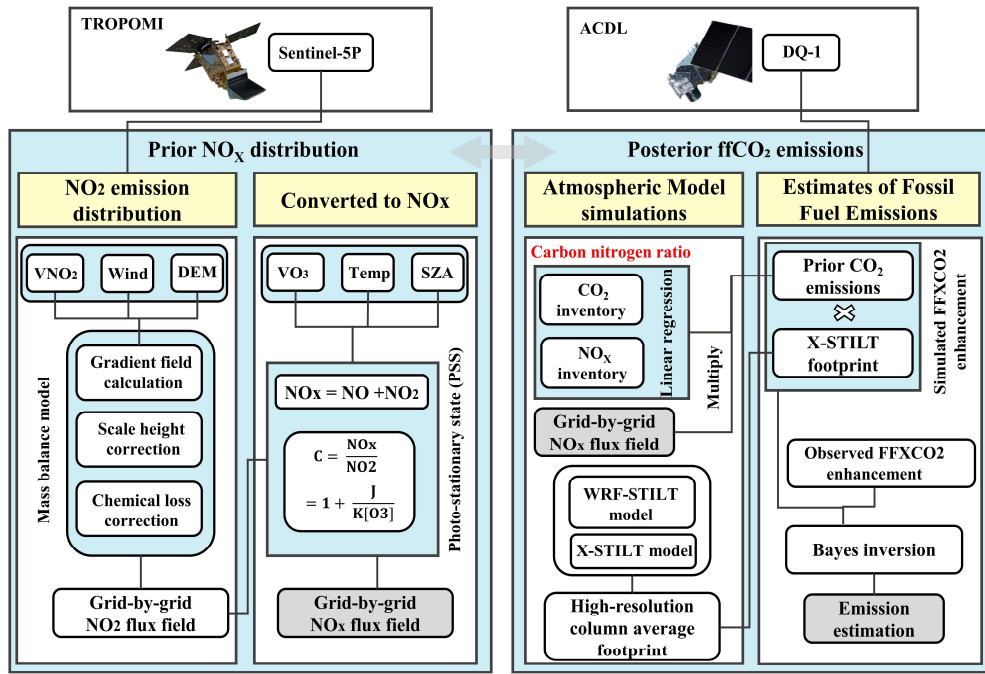
Coupled carbon-nitrogen observations offer a new perspective to address this gap (Reuter et al., 2019; Yang et al., 2023) (Reuter et al., 2019; Yang et al., 2023). Nitrogen oxides (NO<sub>x</sub> = NO + NO<sub>2</sub>) are major co-emitted species from fossil fuel combustion, with emission intensity and spatial distribution closely correlated with ffCO<sub>2</sub> (Feng et al., 2024). Studies have shown that in regions with varying pollution levels, XCO<sub>2</sub> anomalies spatially correlate with tropospheric NO<sub>2</sub> column densities (Hakkarainen et al., 2016). Moreover, the CO<sub>2</sub>-to-NO<sub>x</sub> ratio is often more stable than individual emission amounts because systematic biases in fossil fuel consumption affect both CO<sub>2</sub> and NO<sub>x</sub> statistics (Kononov et al., 2016). Recent research suggests that optimized NO<sub>x</sub> emissions, combined with CO<sub>2</sub>-to-NO<sub>x</sub> ratios from bottom-up inventories, can provide more accurate ffCO<sub>2</sub> estimates (Zheng et al., 2020). For instance, Zheng et al. used TROPOMI NO<sub>2</sub> data to estimate 10-day moving averages of Chinese ffCO<sub>2</sub> emissions during the COVID-19 pandemic, finding an 11.5% decline compared to the same period in 2019 (Zheng et al., 2020). Liu et al. validated the feasibility of NO<sub>x</sub>-based ffCO<sub>2</sub> estimation by comparing inferred CO<sub>2</sub> emissions with highly accurate stack measurements from eight large US

62 power plant(Liu et al., 2020). High-resolution NO<sub>2</sub> column observations, such as those from Sentinel-5P/TROPOMI, can be inverted  
63 using a mass-balance framework to derive accurate NO<sub>x</sub> gridded fluxes(Beirle et al., 2023; Qin et al., 2023; Sun, 2022; Sun et al.,  
64 2021). These NO<sub>x</sub> fluxes can inform the prior spatial allocation of CO<sub>2</sub> emissions due to the co-emission consistency of fossil fuel  
65 sources, and the high temporal resolution of TROPOMI allows rapid updates of CO<sub>2</sub> priors, mitigating the lag inherent in static  
66 inventories(Zhang et al., 2022).

67 The CO<sub>2</sub>-to-NO<sub>x</sub> ratio is crucial for converting NO<sub>x</sub> emissions into ffCO<sub>2</sub> estimates. However, because the CO<sub>2</sub>-to-NO<sub>x</sub> ratio  
68 used in this study is calculated from CO<sub>2</sub> emissions and NO<sub>x</sub> emissions, there is currently a lack of accurate top-down measurement  
69 methods due to measurement limitations, most studies derive this ratio from inventories, and different calculation methods yield significantly different values.  
70 Assimilating observational data to invert CO<sub>2</sub>-to-NO<sub>x</sub> ratios is therefore key to reducing uncertainties in ffCO<sub>2</sub> estimation. Passive  
71 top-down observations are limited by cloud cover, aerosols, and solar irradiance, and in complex multi-source and topographic  
72 environments, signal attribution is challenging, restricting the accuracy and stability of city-scale inversions(Miller et al., 2014).

73 In 2022, China launched DQ-1, the world's first CO<sub>2</sub> lidar satellite, equipped with an IPDA lidar (ACDL) capable of high  
74 signal-to-noise ratio, day-and-night, all-weather observations. The dual-wavelength differential method mitigates interference from  
75 aerosols and thin clouds(Han et al., 2017; Han et al., 2025). Compared to passive satellites, IPDA lidar offers unique advantages in  
76 urban plume detection and fine-scale emission inversion(Kiemle et al., 2017; Kiemle et al., 2011; Yi et al., 2024). Previous studies  
77 using DQ-1 XCO<sub>2</sub> data successfully constrained point-source emissions(Cheng et al., 2025; Han et al., 2024; Zhang et al., 2025),  
78 and Yi et al. developed a kilometer-scale urban flux inversion system based on ACDL measurements, comparing its constraints to  
79 passive systems like OCO-2/3(Yi et al., 2025)(~~Yi et al., 2025~~)(~~Yi et al., 2024~~).

80 In this study, we propose a city-scale ffCO<sub>2</sub> inversion framework that jointly assimilates active and passive satellite observations,  
81 dynamically bridging NO<sub>x</sub> and CO<sub>2</sub> emissions via the CO<sub>2</sub>-to-NO<sub>x</sub> ratio. The workflow is illustrated in Fig. 1. TROPOMI NO<sub>2</sub>  
82 column data are first used to invert NO<sub>x</sub> gridded emissions via a mass-balance approach. Combined with prior CO<sub>2</sub>-to-NO<sub>x</sub> ratios,  
83 these NO<sub>x</sub> fluxes are converted into CO<sub>2</sub> priors. DQ-1 XCO<sub>2</sub>-Lidar along-track measurements are then assimilated using WRF-  
84 STILT high-resolution atmospheric transport simulations within a Bayesian inversion framework to estimate total city emissions  
85 and explicitly quantify observational and transport uncertainties. We applied this approach to Beijing, Paris, and Cairo, representing  
86 cities with diverse topographies and emission patterns, using August 2022 TROPOMI and DQ-1/ACDL data to evaluate the  
87 framework's ability to provide robust, high-resolution urban emission estimates. It is noteworthy that no unified CO<sub>2</sub>-to-NO<sub>x</sub> ratio  
88 calculation method currently exists, and different methods yield divergent values, which can significantly bias final emission  
89 estimates. This study systematically evaluates the influence of prior CO<sub>2</sub>-to-NO<sub>x</sub> ratio calculation methods on inversion outcomes,  
90 demonstrating that Bayesian assimilation can substantially reduce this uncertainty, converging different ratios to a consistent  
91 magnitude. This framework offers a unified approach for estimating urban emissions under limited or uncertain inventory conditions,  
92 providing a timely and reliable method for reporting anthropogenic CO<sub>2</sub> emissions at the city scale.



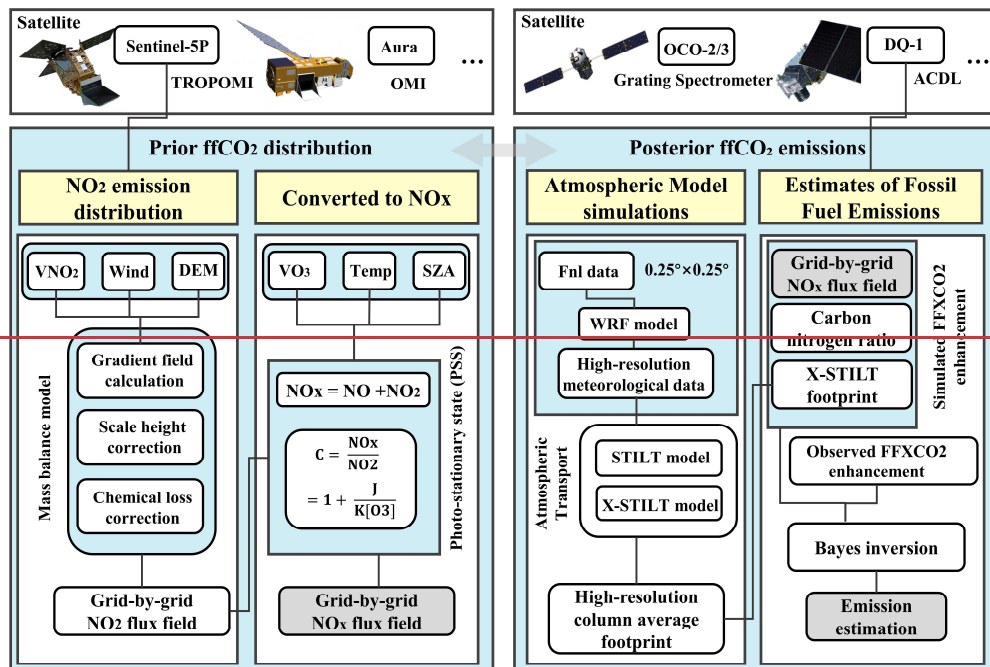


Figure 1 Technical framework diagram

The remainder of this paper is structured as follows. Section 2 introduces the datasets and methods used in this study. Section 3 presents the results of NO<sub>x</sub> emission estimation in Paris, Cairo, and Beijing based on TROPOMI observations combined with a mass-balance approach, followed by city-scale ffCO<sub>2</sub> inversion results obtained by assimilating DQ-1 ACDL observations within a Bayesian framework. Section 4 examines the influence of different prior CO<sub>2</sub>-to-NO<sub>x</sub> ratio calculation methods on the inversion process and highlights the importance of optimizing the CO<sub>2</sub>-to-NO<sub>x</sub> ratio using observational data. Finally, Section 5 summarizes and discusses the potential of the multi-source satellite Bayesian inversion framework for constraining urban CO<sub>2</sub> emissions, and emphasizes the significance of optimized CO<sub>2</sub>-to-NO<sub>x</sub> ratios for improving the accuracy of urban ffCO<sub>2</sub> estimates.

## 2. Materials and methods

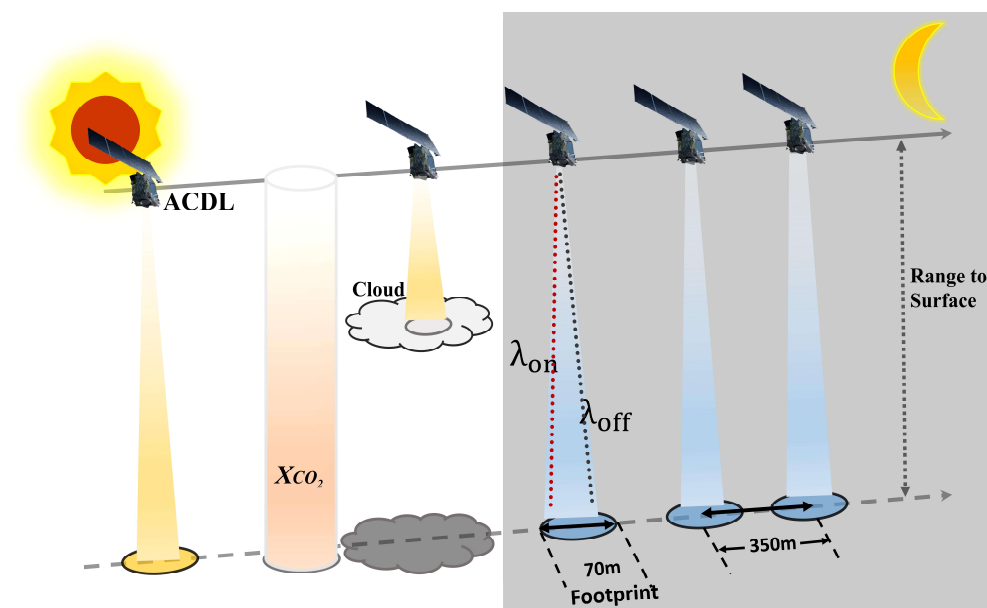
### 2.1. Data

#### 2.1.1. AC DL Productions

The concept of DQ-1 was first proposed in 2012 with the aim of developing a satellite-borne lidar system analogous to the Cloud-Aerosol Lidar with Orthogonal Polarization (CALIOP) onboard CALIPSO, and it was officially approved as a national

108 project in 2017. Unlike conventional environmental monitoring satellites, DQ-1 is distinguished by its breakthrough active remote  
109 sensing payload—the Atmospheric Carbon Dioxide Differential Absorption Lidar (ACDL)—which enables [activedirect](#) “top-down”  
110 observations of atmospheric CO<sub>2</sub>. The ACDL underwent successive stages of laboratory prototype development and airborne  
111 validation before its successful launch onboard the DQ-1 satellite into a near-polar sun-synchronous orbit at an altitude of ~705 km  
112 on April 18, 2022. Operational observations commenced in late May of the same year. This study primarily analyzes data collected  
113 August 2022.

114 The ACDL operates on the principle of Integrated Path Differential Absorption (IPDA) lidar, retrieving atmospheric column-  
115 averaged CO<sub>2</sub> concentrations (XCO<sub>2</sub>) via differential absorption techniques. The inversion methodology and data product  
116 specifications have been described in detail elsewhere; here, we provide only a brief overview (Han et al., 2025). The instrument  
117 transmits two nearly simultaneous laser pulses: one at a strong absorption line of CO<sub>2</sub> (R16, referred to as the “online” wavelength)  
118 and the other at a nearby weak absorption line (the “offline” wavelength). These are stabilized at 6361.225 cm<sup>-1</sup> and 6360.981 cm<sup>-1</sup>,  
119 corresponding to 1572.024 nm and 1572.085 nm, respectively. By comparing the differential attenuation between the online and  
120 offline signals, the system effectively mitigates the influence of aerosols and other interfering species, except water vapor, thereby  
121 enabling accurate retrievals of XCO<sub>2</sub>. The inversion process relies on dedicated algorithms, with the central concept being that the  
122 small wavelength offset produces differential absorption, which enhances the sensitivity of CO<sub>2</sub> detection (details of the ACDL  
123 XCO<sub>2</sub> retrieval algorithm are provided in the Appendix A1).



124 Figure 2 the schematic diagram for DQ-1's detection principle  
125

126

127 Figure 2 illustrates the schematic of the DQ-1 measurement principle. The XCO<sub>2</sub> products generated by ACDL are provided in  
128 a point-sampling mode analogous to that of GOSAT. The lidar records one footprint of approximately 70 m every ~350 m along the  
129 satellite ground track. Additional details of the ACDL operating parameters are provided in the Appendix A1.

### 130 2.1.2. TROPOMI Productions

131 TROPOMI is a nadir-viewing spectrometer onboard ESA's Sentinel-5 Precursor (S5P) satellite, which was launched in October  
132 2017. Operating in an ascending Sun-synchronous polar orbit with an equator crossing time of approximately 13:30 local time,  
133 TROPOMI measures a range of trace gases as well as cloud and aerosol properties across four spectral channels (ultraviolet, visible,  
134 near-infrared, and shortwave infrared). The instrument's minimum pixel size was about  $3.5 \times 7$  km<sup>2</sup> at nadir before being reduced  
135 to  $\sim 3.5 \times 5.5$  km<sup>2</sup> on 6 August 2019 (Veeffkind et al., 2012). In this study, we used the S5P-PAL dataset (consistent with version  
136 2.3.1) (Eskes et al., 2021) covering the period from 1 August to 1 September 2022, obtained from <https://data-portal.s5p-pal.com>

137 To ensure data quality, we filtered out pixels with a `qa_value` < 0.75 (Qin et al., 2023), and, following van Geffen et al., removed  
138 cloudy pixels (cloud radiance fraction > 50%) as well as anomalies (e.g., eclipses) from the TROPOMI NO<sub>2</sub> dataset (Van Geffen et  
139 al., 2022) (Van Geffen et al., 2022a). To test our algorithm framework on a robust dataset, we selected summer NO<sub>2</sub> observations for  
140 three cities located in the mid-latitudes of the Northern Hemisphere, avoiding winter measurements that may be complicated by  
141 potential snow cover. Furthermore, given the need for city-scale accuracy, air mass factor (AMF) corrections were applied locally  
142 following the method described in (Beirle et al., 2023).

143 Sun et al. proposed an oversampling algorithm to project multi-satellite, multi-species observations onto a common grid, with  
144 code publicly available on GitHub ([https://github.com/Kang-Sun-CfA/Oversampling\\_matlab/](https://github.com/Kang-Sun-CfA/Oversampling_matlab/)) (Sun et al., 2018a). In this work, we  
145 applied this algorithm to the pre-processed TROPOMI overpass data, generating oversampled grids at 1 km resolution following  
146 the procedure described in (Sun, 2022).

### 147 2.1.3. Meteorological and DEM data

148 For the estimation of CO<sub>2</sub> emissions through model simulations, we utilized meteorological parameters from the National  
149 Centers for Environmental Prediction Final (NCEP FNL) operational global analysis dataset (National Centers for Environmental  
150 Prediction/National Weather Service/NOAA/U.S. Department of Commerce, 2015). The ds083.3 dataset is provided on a  $0.25^\circ \times$   
151  $0.25^\circ$  latitude-longitude grid and updated every six hours via the Global Data Assimilation System (GDAS)  
152 (<https://rda.ucar.edu/datasets/ds083-3/>). It covers 32 vertical levels, ranging from the surface to the top of the atmosphere, including  
153 the ground level and 31 isobaric layers from 1000 hPa to 1 hPa. Essential variables such as surface pressure, geopotential height,  
154 temperature, relative humidity, and zonal and meridional wind components were used as the main meteorological inputs for driving

155 the WRF-STILT simulations.

156 The wind vector data were obtained from the ERA5 reanalysis dataset (<https://doi.org/10.24381/cds.adbb2d47>)(Hersbach et  
157 al., 2023). We extracted hourly 10 m and 100 m wind vectors at 0.25° spatial resolution for the three selected cities during the period  
158 from 1 August to 1 September 2022. The 10 m wind vectors are used to approximate near-surface winds, whereas the 100 m wind  
159 vectors represent horizontal transport within the planetary boundary layer. These data were averaged to daily values and  
160 subsequently interpolated to match the grid resolution of the column concentration fields described in Section 2.3.1.

161 Digital elevation data were obtained from the GMTED2010 dataset (<https://www.usgs.gov/coastal-changes-and-impacts/gmted2010>)(Danielson and Gesch, 2011). The DEM was resampled and mapped to the same spatial grid as the  
162 concentration and wind fields to ensure consistency across all datasets.  
163

#### 164 **2.1.4. Emissions Inventory**

165 In this study, multiple emission inventories were used to estimate fossil fuel CO<sub>2</sub> (fCO<sub>2</sub>) emissions and to calculate the CO<sub>2</sub>-  
166 to-NO<sub>x</sub> ratio. In the urban observation system simulation experiment (Section 3), the GEMS inventory (0.1° resolution) for NO<sub>x</sub> and  
167 CO<sub>2</sub> emissions(Wang et al., 2013; Huang et al., 2017) was used to derive the prior CO<sub>2</sub>-to-NO<sub>x</sub> ratio (available at:  
168 <https://gems.sustech.edu.cn/data>). For comparison, we also employed the gridded fossil fuel CO<sub>2</sub> emissions inventory from the  
169 Open - source Data Inventory for Atmospheric Carbon dioxide (ODIAC, Version 2024, 1 km resolution;  
170 <https://db.cger.nies.go.jp/dataset/ODIAC/>)(Oda and Maksyutov, 2015). In Section 4, we further utilized the sectoral and 0.1° gridded  
171 NO<sub>x</sub> and CO<sub>2</sub> inventories from the Emissions Database for Global Atmospheric Research (EDGAR;  
172 [https://edgar.jrc.ec.europa.eu/emissions\\_data\\_and\\_maps/](https://edgar.jrc.ec.europa.eu/emissions_data_and_maps/))(Crippa et al., 2018), as well as the sectoral NO<sub>x</sub> and CO<sub>2</sub> inventories from  
173 the Multi-resolution Emission Inventory model for Climate and air pollution research (MEIC; <http://meicmodel.org.cn/>)(Team,  
174 2012). Using different approaches to calculate the CO<sub>2</sub>-to-NO<sub>x</sub> ratio, we quantified the variations arising from different inventory  
175 inputs and assessed their impact on emission inversions.

## 176 **2.2. Methodology**

### 177 **2.2.1. Calculation of Prior Distribution for CO<sub>2</sub> Emissions**

#### 178 **(1) Mass Balance Method**

179 In previous studies, numerous works have detailed the theoretical derivation for inferring gridded fluxes from column  
180 observations(Beirle et al., 2023; Huang et al., 2024; Koene et al., 2024; Qin et al., 2023; Rey-Pommier et al., 2025; Sun, 2022;  
181 Ayazpour et al., 2025)(~~Qin et al., 2023; Beirle et al., 2023; Sun et al., 2018a; Koene et al., 2024; Rey-Pommier et al., 2025; Huang~~  
182 ~~et al., 2024; Sun, 2022; Ayazpour et al., 2025)~~{Ayazpour, 2025 #113}(Sun, 2022; Ayazpour et al., 2025). Such frameworks are

generally based on solutions to the atmospheric continuity equation. Divergence-based approaches typically rely on several key assumptions: (1) exchanges above the planetary boundary layer (column top) and at the surface (column bottom) are neglected, effectively assuming two-dimensional diffusion; (2) horizontal turbulent transport is ignored at coarse grid resolutions; and (3) the deposition term  $S$  is treated using a first-order chemical approximation. Starting from the unsteady, source-driven atmospheric continuity equation, the gridded flux of a given species, such as  $\text{NO}_2$ , can be derived from satellite column observations, with the resulting flux  $\langle E_{\text{NO}_2} \rangle$  expressed as in Equation 1.

$$\langle E_{\text{NO}_2} \rangle = \langle \vec{u} \cdot (\nabla V_{\text{NO}}) \rangle + \frac{\langle V_{\text{NO}} \frac{\partial}{\partial z} (V_{z0}) \rangle}{H} + \frac{\langle V_{\text{NO}} \rangle}{\tau} \quad (1)$$

The detailed derivation is provided in Appendix A2. To fully exploit the available data while accounting for observational errors, spatial gradients were computed along the zonal, meridional, and both diagonal directions. Gradients were numerically approximated using second-order central differences, multiplied by the corresponding decomposed wind vectors, and then averaged. For boundary grid points, one-sided differences were applied.

## (2) Convert $\text{NO}_2$ to $\text{NO}_x$

Nitrogen oxides ( $\text{NO}_x = \text{NO} + \text{NO}_2$ ) do not exist independently in the troposphere, as  $\text{NO}$  and  $\text{NO}_2$  continuously interconvert, while the total  $\text{NO}_x$  remains relatively stable. To convert between  $\text{NO}_2$  column densities and total  $\text{NO}_x$  columns, Sun et al. applied a fixed coefficient of 1.32. In this study, we adopt a more rigorous approach to derive the conversion factor, as expressed in Equation 2 (Beirle et al., 2023), based on the photostationary steady-state assumption:

$$\left\{ \begin{array}{l} V_{\text{NO}_x} = \alpha V_{\text{NO}} = \left(1 + \frac{J}{K X_{\text{O}_3}}\right) V_{\text{NO}_2} \\ J = k_1 * \exp\left(-\frac{k_2}{\cos(\text{SZA})}\right) \\ K = k_3 * \exp\left(-\frac{k_4}{T}\right) \end{array} \right. \quad (2)$$

Here,  $J$  represents the photolysis frequency of  $\text{NO}_2$ , calculated following the methodology in (Dickerson et al., 1982). The rate constants  $k_1$  and  $k_2$  are set to 0.0167 and 0.575, respectively. The solar zenith angle (SZA) can be directly determined from the local latitude, longitude, and time; in this study, SZA values are obtained from the TROPOMI satellite metadata.  $K$  denotes the chemical reaction rate constants for  $\text{NO}$  with  $\text{O}_3$ , expressed in  $\text{cm}^3/(\text{mol}\cdot\text{s})$  and recommended by IUPAC, with  $k_3=2.07*10^{-12}$  and  $k_4=1400$ . The ozone mixing ratio,  $X_{\text{O}_3}$ , is derived from the ESCiMo project (Breninkmeijer and Cai, 2016), and  $T$  represents the boundary-layer mean temperature obtained from ERA5 reanalysis data. Under these definitions, Equation 2 can be rewritten as:

$$X = \alpha * \langle E_{\text{NO}_2} \rangle \quad (3)$$

Using Equation 3 we can obtain grid-resolved estimates of  $\text{NO}_x$  fluxes, which serve as the prior distribution for fossil fuel  $\text{CO}_2$  ( $\text{ffCO}_2$ ) emissions. These estimates provide a data-driven prior inventory for subsequent steps in the inversion framework.

### 209 (3) Scale height and Chemical lifetime

210 Regarding the selection of scale height and first-order chemical lifetime, previous studies, such as Beirle et al., employed fixed  
211 empirical scale height values and adjusted terrain correction terms to obtain optimal estimates(Beirle et al., 2023). Their chemical  
212 lifetime was calculated using a compensation method that accounted for losses integrated over residence times within a 15 km buffer.  
213 While effective at point-source scales, this approach is not directly applicable to our study. In the present work, we follow Sun et  
214 al.'s purely data-driven approach, which leverages observational data without introducing additional assumptions, constructing a  
215 linear regression model to determine these parameters(Sun, 2022). This observation-driven fitting method not only reduces errors  
216 arising from new assumptions but also mitigates biases caused by grid resampling and near-surface wind selection.

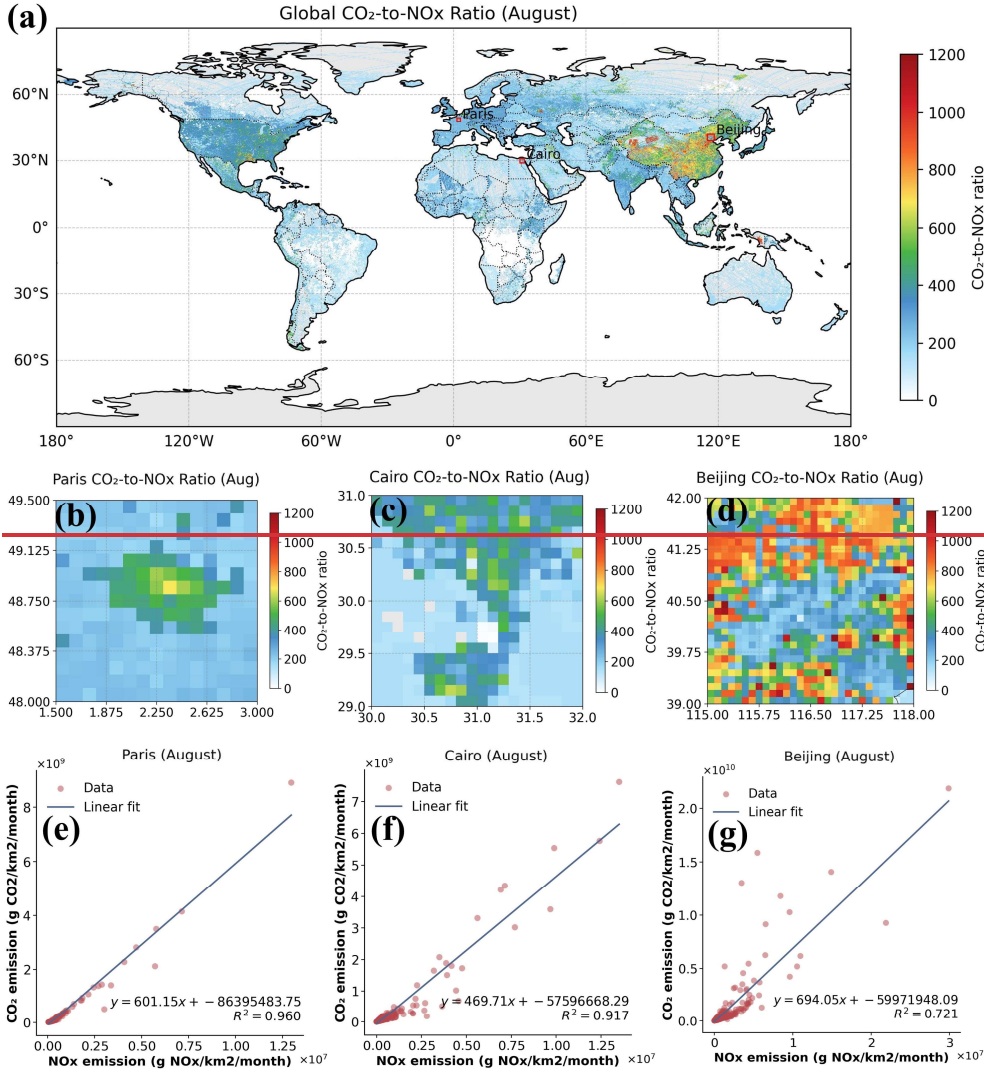
217 To suppress excessive noise in single-day fits, we perform monthly regressions and adopt the temporal and spatial mean over  
218 the month as the final estimate, representing an aggregate over the full spatial domain, the entire month, and the troposphere. The  
219 retrieved scale height and first-order chemical lifetime are then applied back into Equations 4 and 6 to obtain the final gridded  $\text{NO}_x$   
220 vertical fluxes.

221 After terrain correction, the gridded flux fields remove a substantial portion of strong emission signals obscured by wind  
222 divergence and negative divergence artifacts, while the chemical correction term adjusts residual minor negative biases(Sun, 2022;  
223 Sun et al., 2018a; Beirle et al., 2023). Any remaining small negative values after these corrections are set to zero.

### 224 (4) Calculation of Prior $\text{CO}_2$ -to- $\text{NO}_x$ Ratio

225 We used the prior  $\text{CO}_2$ -to- $\text{NO}_x$  ratio in combination with TROPOMI-derived  $\text{NO}_x$  emission distributions to obtain an initial  
226 characterization of urban prior  $\text{ffCO}_2$  emissions. Following the approach of Feng et al., who calculated the  $\text{CO}_2$ -to- $\text{NO}_x$  ratio by  
227 dividing gridded  $\text{CO}_2$  and  $\text{NO}_x$  emission inventories(Feng et al., 2024), we derived city-specific prior  $\text{CO}_2$ -to- $\text{NO}_x$  ratio using the  
228  $0.1^\circ$   $\text{CO}_2$  and  $\text{NO}_x$  inventories from GEMS (<https://gems.sustech.edu.cn/data/database>). Unlike Feng et al., who focused on grid-  
229 level  $\text{CO}_2$ -to- $\text{NO}_x$  ratio, we fitted the gridded ratios across each study region to obtain an integrated city-level  $\text{CO}_2$ -to- $\text{NO}_x$  ratio,  
230 which is more suitable for subsequent inversion analyses (Fig. 3). Details on the associated uncertainties are provided in Section  
231 4.1.

232 Figure 3 illustrates our method for calculating the prior  $\text{CO}_2$ -to- $\text{NO}_x$  ratio. By fitting the  $0.1^\circ$  gridded ratios for each city, we  
233 obtained overall city-scale values. The coefficients of determination ( $R^2$ ) for Paris, Cairo, and Beijing were 0.96, 0.917, and 0.76,  
234 respectively.



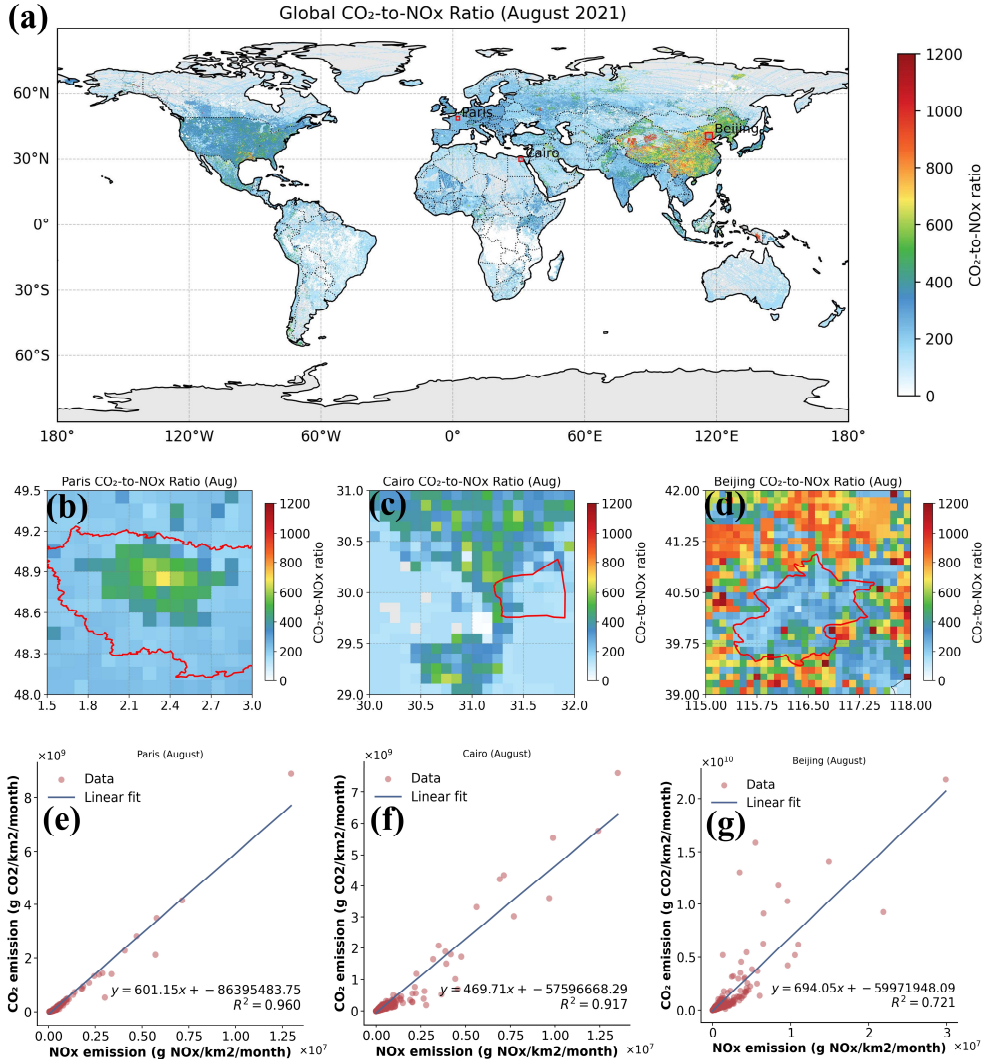


**Figure 3** Schematic diagram of prior CO<sub>2</sub>-to-NO<sub>x</sub> ratio calculation methods. Panel (a) shows the global gridded CO<sub>2</sub>-to-NO<sub>x</sub> ratio derived from GMES data. Panels (b)–(d) present the gridded CO<sub>2</sub>-to-NO<sub>x</sub> ratio for Paris, Cairo, and Beijing (the red lines indicate the boundaries of each city). Panels (e)–(g) display the overall CO<sub>2</sub>-to-NO<sub>x</sub> ratio fitting results for the three cities. We used the Île-de-France administrative boundary to depict Paris in the figures, rather than the city proper. Although our actual study area only covers a subset of Île-de-France (1.5–3° E, 48–49.5° N) Schematic diagram of prior CO<sub>2</sub>-to-NO<sub>x</sub> ratio calculation methods. Panel (a) shows the global gridded CO<sub>2</sub>-to-NO<sub>x</sub> ratio derived from GMES data. Panels (b)–(d) present the gridded CO<sub>2</sub>-to-NO<sub>x</sub> ratio for Paris, Cairo, and Beijing. Panels (e)–(g) display the overall CO<sub>2</sub>-to-NO<sub>x</sub> ratio fitting results for the three cities.

Recently, an increasing number of studies have employed NO<sub>x</sub> emissions to estimate ffCO<sub>2</sub> emissions (Feng et al., 2024; Zheng

域代码已更改

et al., 2020; Xu et al., 2025; Yang et al., 2023; Berezin et al., 2013; Zhang et al., 2022). In inversion methods based on  $\text{NO}_x$  emissions, the choice of the prior  $\text{CO}_2$ -to- $\text{NO}_x$  ratio directly affects the emission estimates. Uncertainty in the prior ratio propagates to the estimated  $\text{ffCO}_2$  emissions, influencing both their magnitude and spatial distribution. To evaluate this effect, we selected several widely used  $\text{CO}_2$ -to- $\text{NO}_x$  ratio calculation methods and systematically assessed their associated uncertainties (results see Section 4.1 and Appendix A6).

- M.1 Grid-level  $\text{CO}_2$ -to- $\text{NO}_x$  ratio derived directly from gridded  $\text{CO}_2$  and  $\text{NO}_x$  inventories (Feng et al., 2024). Since this study scales emissions to the city level, we further fitted the grid-level ratios to obtain city-integrated  $\text{CO}_2$ -to- $\text{NO}_x$  ratios. M.1 calculations were based on the GEMS gridded inventory.

- M.2  $\text{CO}_2$ -to- $\text{NO}_x$  ratios calculated using sectoral emission factors for  $\text{CO}_2$  and  $\text{NO}_x$  (Zheng et al., 2020). We derived city-scale ratios by aggregating across all sectors. M.2 used the GEMS sectoral inventory.

- M.3  $\text{CO}_2$ -to- $\text{NO}_x$  ratios derived from near-real-time satellite observations. Background-stable  $\text{NO}_x$  plumes were used to constrain  $\text{CO}_2$  plumes, and joint fitting of the two concentrations was performed using the cross-sectional flux method (Xu et al., 2025; Reuter et al., 2019). The  $\text{CO}_2$ -to- $\text{NO}_x$  ratio was obtained directly from the half-width at half-maximum. Following this approach, we used TROPOMI and OCO-2 observations to calculate city-scale ratios.

- M.4 Same as M.2, but the MEIC sectoral inventory was used for Beijing.

- M.5 Same as M.1, but calculations were based on the EDGAR gridded inventory.

- M.6 Same as M.2, but calculations were based on the EDGAR sectoral inventory.

## 2.2.2. Estimating $\text{ffCO}_2$ emissions by WRF-STILT simulations

### (1) Quantifying $\text{ffXCO}_2$ enhancements

Distinguishing anthropogenic emission signals from the surrounding “clean” background in  $\text{XCO}_2$  observations is a central challenge for constraining urban carbon emissions via satellite. Definitions of “background” vary across studies. In this work, we define the background as atmospheric  $\text{XCO}_2$  that is unaffected by local emissions within the study region. Following the approach proposed by (Ye et al., 2020) in constraining urban emissions using OCO-2 observations, we adopt a baseline calculation strategy that incorporates latitudinal gradients.

In this framework,  $\text{XCO}_2$  is decomposed into two components:  $\text{XCO}_{2,trend}$ , representing the regional-scale, non-local trend, and  $\text{XCO}_{2,local}$ , whose standard deviation  $\sigma_{local}$  characterizes local-scale variability. Samples satisfying  $\text{XCO}_2 < \text{XCO}_{2,trend} + 0.5\sigma_{local}$  are selected as “background samples,” as they exhibit lower local spatial variability compared with data influenced by fossil fuel emissions. These background samples are then subjected to linear regression to derive the background baseline and

带格式的: 列表段落, 项目符号 + 级别: 1 + 对齐位置: 0 厘米 + 缩进位置: 0.63 厘米

characterize its spatial variation.

## (2) X-Stochastic Time-Inverted Lagrangian Transport model for ACDL productions

We employ the X-STILT V1 model to trace CO<sub>2</sub> concentration variations driven by prior emission information. X-STILT integrates satellite profile data and enables a comprehensive uncertainty assessment of urban XCO<sub>2</sub> enhancements on a per-observation basis (Wu et al., 2018). Originally developed to extract urban signals from passive OCO-2 XCO<sub>2</sub> observations, we have adapted the framework for use with the active CO<sub>2</sub> satellite DQ-1, with appropriate modifications. The relationship between XCO<sub>2</sub><sup>Lidar</sup> (DQ-1 XCO<sub>2</sub> observations) measurements and the CO<sub>2</sub> vertical profile, CO<sub>2</sub>(p), can be formulated as follows:

$$XCO_2^{Lidar} = \frac{\int_{p_{surface}}^{p_{toa}} CO_2(p) WF(p) dp}{\int_{p_{surface}}^{p_{toa}} WF(p) dp} = \sum_{n=1}^{toa} \frac{WF(p_n)}{IWF} \cdot CO_2(p_n) \quad (4)$$

Here,  $p_{toa}$  represents the pressure at the bottom height of the ACDL, and  $p_{surface}$  represents the pressure corresponding to the surface elevation at the laser footprint.  $WF$  and  $IWF$  denote the weighting function and the normalized weighting function of the ACDL, respectively. A detailed description is provided in Appendix A1.

设置了格式: 字体: (默认) Times New Roman, (中文) 宋体, 非倾斜

We approximate the CO<sub>2</sub> concentration by summing the background concentration with the simulated ffCO<sub>2</sub> enhancement. Here, the simulated ffCO<sub>2</sub> enhancement,  $\Delta CO_2^{ffCO_2}(p) = \langle ffCO_2, foot(p) \rangle$ , is obtained by interpolating the modeled ffCO<sub>2</sub> fluxes along tracer-tagged footprints. Consequently, the relationship between the ffCO<sub>2</sub> fluxes and the simulated XCO<sub>2</sub><sup>Lidar</sup><sub>mod</sub>, is established, yielding the modeled fossil fuel CO<sub>2</sub> enhancement XCO<sub>2</sub><sup>Lidar</sup><sub>ffCO<sub>2</sub>, mod</sub> along the lidar track:

$$XCO_2^{Lidar}_{ffCO_2, mod} = XCO_2^{Lidar}_{mod} - XCO_2^{Lidar}_{background} = \sum_{n=1}^{toa} \frac{WF(p_n)}{IWF} \cdot \langle emissions, foot(p_n) \rangle \quad (5)$$

XCO<sub>2</sub><sup>Lidar</sup><sub>background</sub> represents the background concentration along the selected DQ-1 orbit (see Section 2.2.2 (1)). The operator  $\langle, \rangle$  denotes an inner product,  $emissions_{ffCO_2}$  is the prior emission flux, and  $foot(p_n)$  represents the modeled footprint at different vertical layers. Using the above formulation, the mathematical foundation for the inversion is established. By integrating footprints across multiple release heights, the equation can be further simplified. In this study, we define the ffXCO<sub>2</sub> enhancement simulated via the atmospheric transport model as:

$$XSTILT^{Lidar} = \sum_{n=1}^{toa} \frac{WF(p_n)}{IWF} \cdot foot(h_n) \quad (6)$$

$$XCO_2^{Lidar}_{ffCO_2, mod} = \langle XSTILT^{Lidar}, emissions \rangle \quad (7)$$

Here, XSTILT<sup>Lidar</sup> is defined as the column-averaged footprint, corresponding to the column-averaged CO<sub>2</sub> concentration. The inner product of the column-averaged footprint and the prior emission flux yields the simulated XCO<sub>2</sub> enhancement.

### (3) Bayes inversion

We used the  $\text{NO}_x$  emissions obtained previously as prior fluxes and, through the  $\text{CO}_2$ -to- $\text{NO}_x$  ratio, established the relationship between the prior emissions and the  $\text{XCO}_2$  observed by DQ-1 (Equation 9). The  $\text{XCO}_2$  enhancements estimated from DQ-1 observations were then employed to impose “top-down” constraints on the simulated results. Following the approaches of (Che et al., 2024; Ye et al., 2020; Wang et al., 2014; Sheng et al., 2025), we applied a Bayesian inversion framework to optimize the prior emission estimates.

$$y_{obs} = y_{sim} \cdot \lambda + \varepsilon_p \quad (8)$$

Here,  $y_{obs}$  and  $y_{sim}$  represent the observed  $\text{fXCO}_2$  enhancements and the simulated  $\text{NO}_x$  enhancements, respectively. The symbol  $\lambda$  denotes the  $\text{CO}_2$ -to- $\text{NO}_x$  ratio, and  $\varepsilon_p$  represents the observational error, which encompasses contributions from DQ-1 measurement uncertainties, model errors, and errors in model parameters. It is defined as follows:

$$\begin{cases} y_{obs} = \int_{latitude}^{latitude2} ffXCO2_{obs} dt \\ y_{sim} = \int_{latitude1}^{latitude2} < X, footprint > dt \end{cases} \quad (9)$$

$$\varepsilon_{obs} = \sqrt{\sigma_{measurement}^2 + \sigma_{sim}^2} \quad (10)$$

In this context,  $\text{fXCO}_2_{obs}$  represents the DQ-1  $\text{XCO}_2$  enhancement after background concentration removal. The notation  $< X, footprint >$  denotes the simulated  $\text{NO}_x$  enhancement, obtained by convolving the  $\text{NO}_x$  emission inventory  $X$  with the STILT-derived footprint (It should be noted that the footprints used here represent hourly footprints during the simulation period, whereas the  $\text{NO}_x$  emissions are monthly emissions derived using the method described in Section 2.2.1. Therefore, we use the New High Resolution Temporal Profiles in EDGAR dataset ([https://edgar.jrc.ec.europa.eu/dataset\\_temp\\_profile](https://edgar.jrc.ec.europa.eu/dataset_temp_profile)) to distribute the monthly  $\text{NO}_x$  emissions to each hourly footprint). Pseudo-observations,  $\text{fXCO}_2_{obs}$ , are generated by averaging DQ-1 measurements over one-second intervals along the satellite track (~7 km), together with the corresponding simulated values.

Following the Bayesian inversion approach, the state vector  $\lambda$  is expressed in terms of the  $\text{CO}_2$ -to- $\text{NO}_x$  ratio, representing the relationship between urban fossil fuel  $\text{CO}_2$  and  $\text{NO}_x$  emissions. The Jacobian matrix is derived from the simulated  $\text{NO}_x$  enhancement  $y_{sim}$ . Here,  $\sigma_{measurement}^2$  represents the observational error variance, and  $\sigma_{sim}^2$  denotes the model transport error variance. DQ-1 observations are assumed unbiased with respect to the true state. To account for measurement uncertainty, random Gaussian noise with a standard deviation of 0.3 ppm—representing the lower limit of observational error—is added to the observations.

By minimizing the loss function, we obtain the posterior  $\text{CO}_2$ -to- $\text{NO}_x$  ratio  $\hat{\lambda}$  and posterior uncertainty  $\hat{\sigma}$  :

$$\hat{\lambda} = \lambda + \sigma_{sim}^2 y_{sim}^T (y_{sim} S_{obs} y_{sim}^T + S_{obs})^{-1} (y_{obs} - y_{sim} \lambda) \quad (11)$$

$$\hat{\sigma}^2 = (y_{sim}^T S_{obs}^{-1} y_{sim} + \sigma_{sim}^{-2})^{-1} \quad (12)$$

Here,  $S_{obs}$  is a diagonal matrix, with the diagonal entries representing the observational error variances  $\varepsilon_{obs}^2$  for each orbit. the prior uncertainty  $\sigma_{sim}$  is primarily derived from the uncertainties in the prior NO<sub>x</sub> emission distribution  $\sigma_{NOx}$  and the prior CO<sub>2</sub>-to-NO<sub>x</sub> ratio  $\sigma_{C/N}$  as equation 13:

$$\sigma_{sim} = \sqrt{\sigma_{NOx}^2 + \sigma_{C/N}^2} \quad (13)$$

### 3. Urban Observation System Simulation Experiment

#### 3.1. Satellite-driven urban NO<sub>x</sub> emission distribution

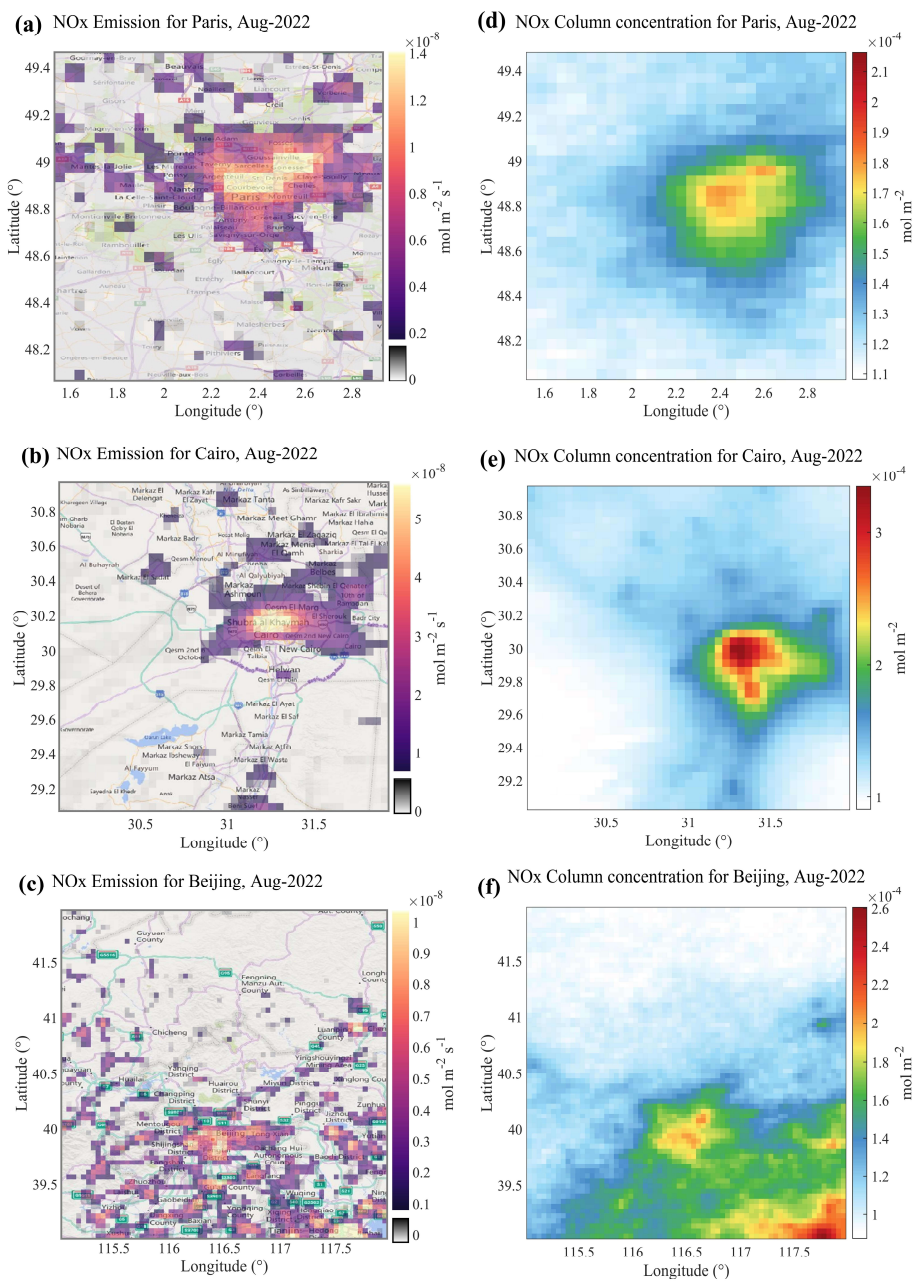
As described in Section 2.2.1, we applied the mass balance approach in the three cities to derive prior NO<sub>x</sub> gridded inventories, which serve as the basis for constructing ffCO<sub>2</sub> gridded emissions. The grid resolution was set to 5 km × 5 km. Figure 4 illustrates the detailed NO<sub>x</sub> fluxes for August 2022 over Beijing, Paris, and Cairo, produced entirely via a top-down approach, with panels (a)–(c) corresponding to Beijing, Paris, and Cairo, respectively.

From the figure, it is evident that the average NO<sub>x</sub> flux magnitude in all three cities is on the order of ~10<sup>-8</sup> mol m<sup>-2</sup> s<sup>-1</sup>. However, their spatial distributions differ considerably. Both Paris and Cairo exhibit highly concentrated emission patterns. In Cairo, the central urban area and industrial zones display peak NO<sub>x</sub> fluxes on the order of ~10<sup>-7</sup> mol m<sup>-2</sup> s<sup>-1</sup>. These high-flux regions sharply decrease with distance from the center, highlighting a pronounced urban boundary effect. In contrast, Beijing not only exhibits strong emissions in the central urban area (within the Sixth Ring Road) but also features numerous dispersed point- and area-like sources in suburban districts (e.g., Fangshan in the southwest) and in the surrounding hills and mountains. Compared with Cairo's concentrated emissions, Beijing's peak NO<sub>x</sub> grid flux in the urban core is nearly one order of magnitude lower (see the color scale mapping in Fig. 4); however, due to the city's larger spatial extent, the total flux remains substantially higher than that of Cairo.

Beijing's topography, with higher elevations in the northwest and lower elevations in the southeast, can induce local wind divergence over hilly and mountainous areas. This effect may generate false positives when using the divergence method (Sun et al., 2021; Liu et al., 2021). In the northwestern suburban mountains of Beijing, the mean wind divergence can reach magnitudes of ~ ±10<sup>-4</sup> s<sup>-1</sup>, while TROPOMI NO<sub>2</sub> column densities are on the order of 10<sup>-4</sup> mol m<sup>-2</sup>. Such magnitudes are comparable to mid-scale urban averages or point-source emissions. Neglecting the divergence term can result in genuine emissions being omitted, while background fluxes induced by terrain or wind divergence are mistakenly included. Following (Sun, 2022), we applied Eq. A5 to reconstruct the wind-divergence term using surface wind and terrain gradients, thereby reintegrating previously neglected area-like emissions. Using Beirle et al.'s methodology, we integrated the net gridded fluxes within a 60 km radius centered on Beijing over

352 the entire year of 2022 to estimate the city's annual NO<sub>x</sub> emissions at 251,450 t. This value is approximately 9.7% higher than the  
353 2022 annual emission reported in the MEIC inventory for Beijing (227,000 t). Although the total magnitude is consistent, the spatial  
354 distribution from top-down estimates differs substantially from bottom-up inventories. Section 3.2.2 further analyzes these  
355 differences by simulating urban ffCO<sub>2</sub> plumes using both our ffCO<sub>2</sub> inventory and the ODIAC inventory.

356 By comparison, Paris and Cairo are situated on relatively flat terrain (maximum elevation ~180 m). Terrain-induced wind  
357 divergence is negligible relative to total fluxes (wind-terrain and divergence contributions  $\sim 10^{-10}$  mol m<sup>-2</sup> s<sup>-1</sup>), leaving the continuity  
358 equation primarily governed by wind-weighted column gradients. Cairo, located upstream of the Nile Delta in a high-albedo desert  
359 region, benefits from low uncertainty in satellite-derived NO<sub>2</sub> columns. Under these conditions, the top-down NO<sub>x</sub> inventory closely  
360 aligns with the bottom-up inventory in terms of spatial distribution. Paris, situated in the Paris Basin along the Seine River,  
361 experiences minimal terrain gradients. Although less extreme than Cairo, the slight topographic variation still produces pronounced  
362 urban boundary effects in the inversion results.



363

364

365

Figure 4 Gridded prior NO<sub>x</sub> emission inventories derived from the mass balance method. Panels (a)–(c) show the NO<sub>x</sub> flux distributions (unit: mol/m<sup>2</sup>/s) for Beijing, Paris, and Cairo in August 2022. Panels (d)–(f) present the resampled monthly mean NO<sub>2</sub> column

concentration distributions for the three cities. Basemap for panels (a)–(c): Esri World Topographic Map. Sources: Esri, HERE, Garmin, Intermap, INCREMENT P, GEBCO, USGS, FAO, NPS, NRCAN, GeoBase, IGN, Kadaster NL, Ordnance Survey, Esri Japan, METI, Mapwithyou, NOSTRA, © OpenStreetMap contributors, and the GIS user community.

To quantitatively compare the NO<sub>x</sub> emission characteristics and atmospheric behavior among Beijing, Paris, and Cairo, derived using the mass balance approach, we analyzed key parameters for August, including mean NO<sub>x</sub> fluxes, total emissions, chemical lifetimes, vertical distribution scale heights, and NO<sub>x</sub>/NO<sub>2</sub> ratios (Table 1). These NO<sub>x</sub> behavior parameters reflect heterogeneous characteristics shaped by the interplay of emission intensity, photochemical conditions, and boundary layer structure.

In terms of mean NO<sub>x</sub> flux per unit area (mol m<sup>-2</sup> s<sup>-1</sup>), Cairo exhibits the highest value (0.35 × 10<sup>-8</sup>), followed by Paris (0.28 × 10<sup>-8</sup>) and Beijing (0.24 × 10<sup>-8</sup>), indicating a higher concentration-emission of urban emission sources in Cairo—particularly from traffic—resulting in stronger NO<sub>x</sub> release per unit surface area. Nevertheless, Beijing’s total NO<sub>x</sub> emissions (182,800 t yr<sup>-1</sup>) are substantially higher than those of the other two cities, reflecting its larger urban extent and greater overall emission intensity, characteristic of a complex multi-source emission profile.

The first-order chemical lifetime of NO<sub>x</sub> in the atmosphere indicates its removal rate and is influenced by factors such as OH radical concentration and solar radiation intensity. Paris exhibits the longest NO<sub>x</sub> chemical lifetime (6.91 h), followed by Beijing (4.70 h) and Cairo (2.93 h). These differences are closely linked to photochemical activity: strong summer sunlight and high temperatures in Cairo enhance OH-driven removal reactions, whereas the relatively mild mid-latitude climate of Paris, combined with emission control measures, prolongs NO<sub>x</sub> lifetime.

Regarding vertical distribution, the NO<sub>x</sub> scale height also varies across the three cities. Beijing shows the highest scale height (2.08 km), reflecting the combined effects of strong convective transport and multi-source emissions that elevate NO<sub>x</sub> into the upper mixing layer. By contrast, Cairo (1.41 km) and Paris (1.21 km) display more typical boundary-layer-constrained distributions, indicating that ground-level emission controls and thermal structure strongly modulate vertical NO<sub>x</sub> transport.

Finally, the NO<sub>x</sub>/NO<sub>2</sub> ratio provides insight into the proportion of NO and its degree of conversion. Beijing exhibits the highest ratio (1.41), followed by Cairo (1.32) and Paris (1.29), suggesting a higher fraction of NO in Beijing, likely associated with dense traffic sources and a larger fraction of primary NO emissions. The relatively lower ratio in Paris reflects a higher NO<sub>2</sub> fraction, consistent with effective emission controls and extensive photochemical conversion.

**Table 1** Grid-averaged NO<sub>x</sub> fluxes, with total urban NO<sub>x</sub> emissions as intermediate parameters in the mass balance method.

City	NO <sub>x</sub> average flux mol/(m <sup>2</sup> * s)	NO <sub>x</sub> total emission kt/month	Chemical lifetime(hour)	Scale height(km)	NO <sub>x</sub> /NO <sub>2</sub>
Beijing	0.235 10 <sup>-8</sup>	15.29	4.69	2.07	1.41

Paris	0.277 10 <sup>-8</sup>	4.45	6.90	1.21	1.29
Cairo	0.353 10 <sup>-8</sup>	6.78	2.93	1.40	1.32

[Details of the uncertainties are provided in the Appendix A5.](#)

设置了格式: 字体: (中文) Times New Roman, 9 磅, 加粗

设置了格式: 字体: (中文) Times New Roman, 9 磅, 加粗

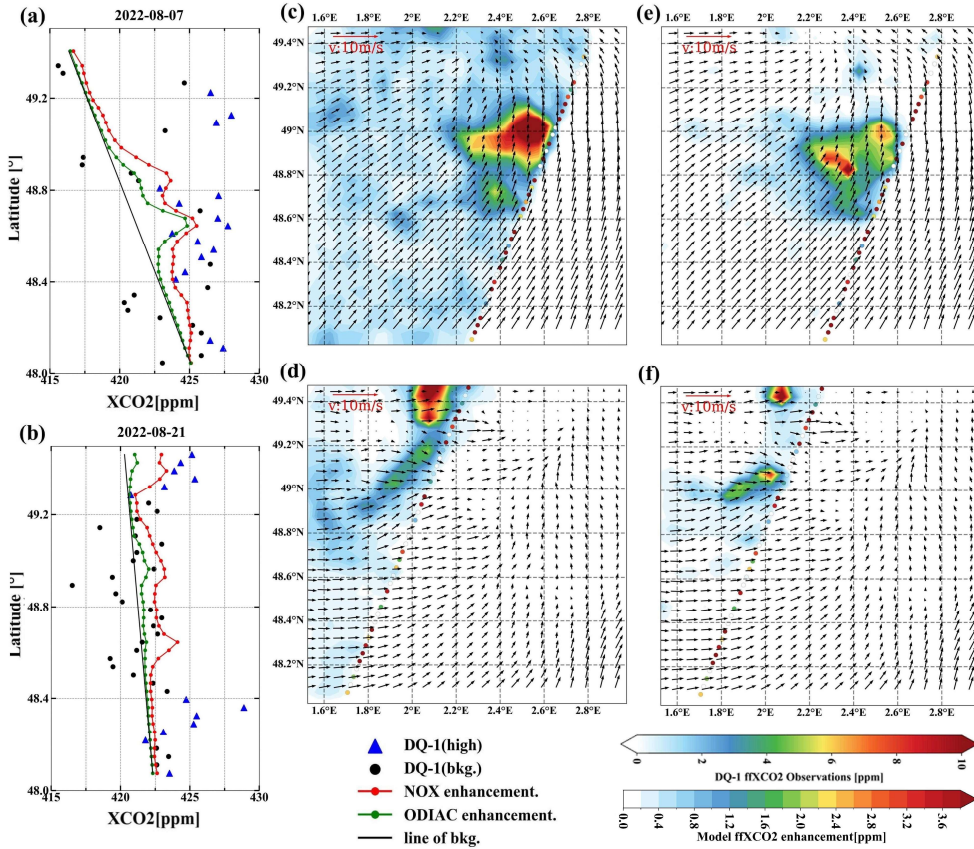
### 3.2. Urban Fossil Fuel XCO<sub>2</sub> Enhancement (ffXCO<sub>2</sub>)

In this section, we summarize the prior ffXCO<sub>2</sub> emissions for each study region. For the selected orbits, the total monthly emissions of Beijing, Paris, and Cairo were approximately 7.47–9.94, 2.91–3.33, and 2.73–3.60 MtC/month, respectively. To constrain emissions, we compared observed and simulated ffXCO<sub>2</sub> enhancements, where ffXCO<sub>2</sub> enhancement is defined as the increase in XCO<sub>2</sub> relative to the background level caused by local fossil fuel emissions. The prior ffXCO<sub>2</sub> enhancements were simulated by taking the inner product of prior NO<sub>x</sub> emissions inventories with STILT footprints, while the observed enhancements from DQ-1 were derived by subtracting the background concentration from the measured XCO<sub>2</sub>. By comparing prior and observed ffXCO<sub>2</sub> enhancements, we assessed the variability of ffXCO<sub>2</sub> along the orbit and investigated the sources and detectability of the ffXCO<sub>2</sub> signal.

#### 3.2.1. Comparison of Modeled and Observed ffXCO<sub>2</sub>

Complex horizontal wind fields can lead to elongated and non-Gaussian plume structures in simulated ffXCO<sub>2</sub> distributions (Ye et al., 2020). This feature is illustrated in Fig. 5c–f. Figures 5a and 5b show the simulated and observed XCO<sub>2</sub> along two overpasses (simulated XCO<sub>2</sub> is obtained by adding the simulated ffXCO<sub>2</sub> to the background derived in Section 2.2.2 (1)). Along these overpasses, ffXCO<sub>2</sub> enhancements exceeding 5 and 10 ppm were observed, with the measured enhancements consistently larger than the simulated values. Although the simulated peak on 7 August is narrower than the observed peak, and the observed peak near 48.4° on 21 August shows a ~0.3° displacement relative to the simulation, the overall magnitude of simulated ffXCO<sub>2</sub> agrees well with observations.

To further evaluate the feasibility of constraining fossil fuel CO<sub>2</sub> emissions using the NO<sub>x</sub> inventory, we performed a comparative analysis using the ODIAC inventory. We compared simulated ffXCO<sub>2</sub> during the satellite overpasses based on the NO<sub>x</sub> and ODIAC inventories (colored shaded areas in the figure), as well as their contributions to the pseudo-observed XCO<sub>2</sub> at the satellite locations (colored dots), where the red line represents enhancements derived from the NO<sub>x</sub> inventory and the green line represents those from ODIAC. Over Paris, the NO<sub>x</sub>-based simulation yields higher ffXCO<sub>2</sub> enhancements than ODIAC, likely due to uncertainty in the prior CO<sub>2</sub>-to-NO<sub>x</sub> ratio. Nonetheless, both inventories capture enhancements exceeding 4 ppm. Moreover, the line plots indicate that the temporal variation and magnitude of the simulated concentration contributions (red and green lines) are nearly identical.

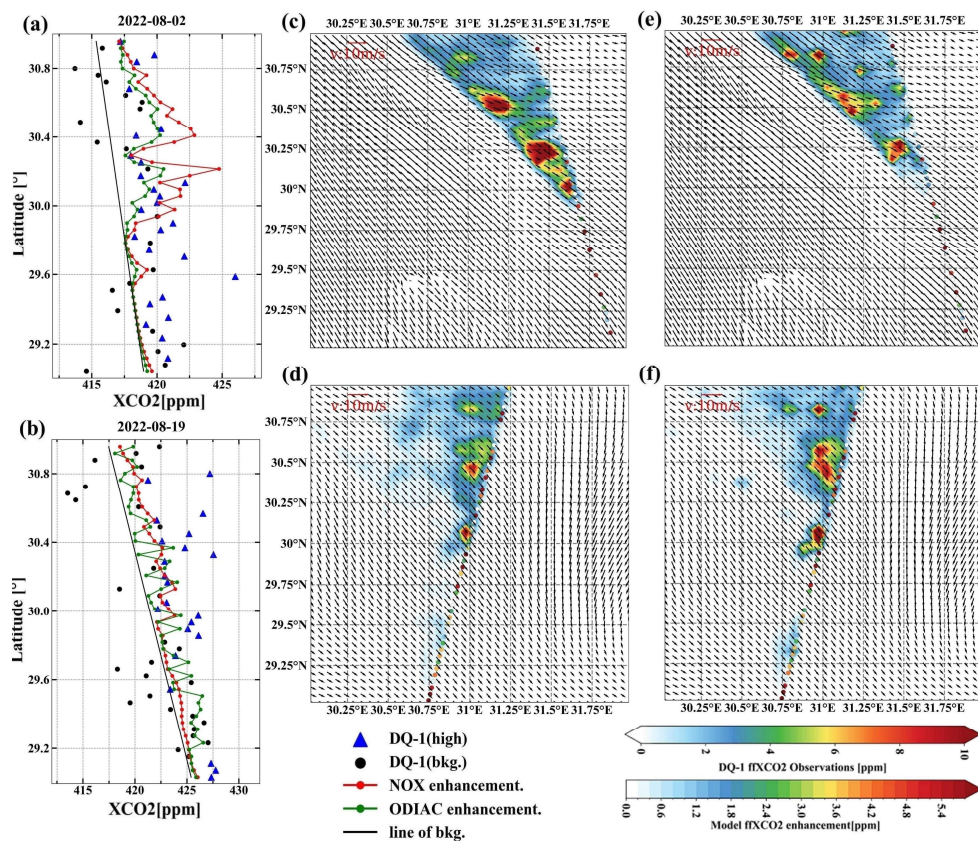


420  
421 **Figure 5** Comparison between simulated and observed fFXCO<sub>2</sub> enhancements using DQ-1 overpasses above Paris on 7 August 2022 and  
422 21 August 2022 at 01:00 UTC. Panels (a) and (b) show DQ-1 XCO<sub>2</sub> along the two tracks (black dots and blue triangles) and simulated  
423 XCO<sub>2</sub> (red solid line: sum of background concentration and fFXCO<sub>2</sub> simulated using the NO<sub>x</sub> emissions; green solid line: sum of  
424 background concentration and fFXCO<sub>2</sub> simulated using the ODIAC inventory), averaged over 0.5 s. Black circles denote the data used to  
425 derive the background concentration (black solid line). Panels (c)–(f) show simulated fFXCO<sub>2</sub> and observed fFXCO<sub>2</sub> retrieved from DQ-1  
426 data ((c), (d): based on the NO<sub>x</sub> inventory; (e), (f): based on the ODIAC inventory). Background XCO<sub>2</sub> concentrations have been subtracted.  
427 The reference vector indicates a wind speed of 10 m/s.

428  
429 We examined local fFXCO<sub>2</sub> enhancements during two overpasses of Cairo on 2 August 2022 at 11:00 and 19 August 2022 at  
430 23:00. As shown in Fig. 6, the simulated fFXCO<sub>2</sub> peaks exceed 6 ppm. In contrast to Paris, where enhancements are widespread,  
431 diffuse, and lack clear structure, and Beijing, where plumes exhibit complex patterns, the simulated fFXCO<sub>2</sub> over Cairo is strongly  
432 influenced by northwesterly winds, resulting in well-defined plumes. Figure 5a illustrates that the simulations based on both  
433 inventories on 2 August produce similar magnitudes and trends, consistent with the Paris results, where the NO<sub>x</sub>-based simulation

434 exceeds that from ODIAC. Notably, the simulated peaks on 2 August also show a spatial offset relative to the observations.  
 435 Following Ye et al. 2020, such offsets are attributed to the satellite trajectory crossing the plume edges nearly parallel to the plume  
 436 axis, making the simulated fXCO<sub>2</sub> highly sensitive to errors in the horizontal wind field.

437 Notably, the overpasses above Paris and Cairo (Figs. 5a and 6b) exhibit higher latitudinal gradients in the background XCO<sub>2</sub>,  
 438 as indicated by the background lines. The approach used to derive these background lines provides a reliable estimate of background  
 439 XCO<sub>2</sub> because, within the relevant regions, the observed and modeled cumulative fXCO<sub>2</sub> enhancements along the satellite track  
 440 are largely consistent. Consequently, these findings highlight the effectiveness of the background line method for inferring satellite-  
 441 observed background XCO<sub>2</sub>. They also emphasize that the spatial scale of satellite data analysis is closely linked to the constraints  
 442 imposed by local emission sources. Neglecting the latitudinal gradient of background XCO<sub>2</sub> may introduce biases in the estimation  
 443 of fXCO<sub>2</sub> and, consequently, in derived emission fluxes (Ye et al., 2020).

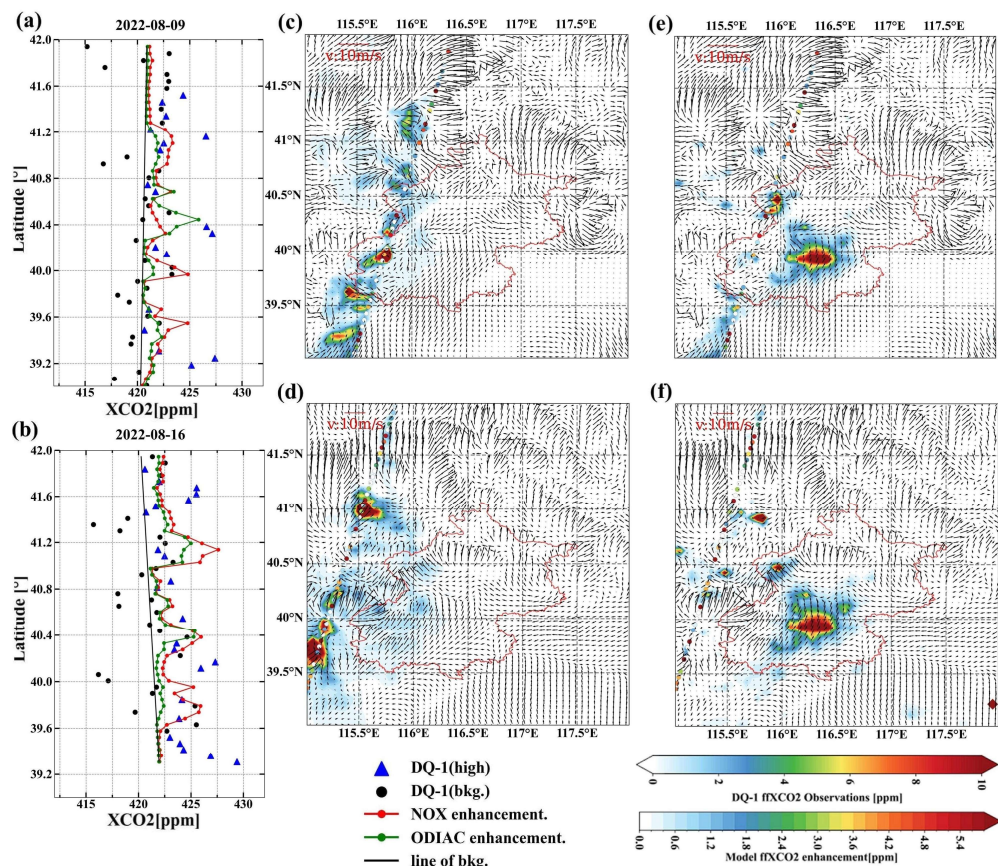


444  
 445 **Figure 6** Similar to Fig. 5, comparison between simulated and observed fXCO<sub>2</sub> enhancements using DQ-1 overpasses above Cairo on 2  
 446 August 2022 at 11:00 UTC (panels a, c, e) and 19 August 2022 at 23:00 UTC (panels b, d, f). Panels (c) and (d) show the simulated fXCO<sub>2</sub>

447 enhancements based on the NO<sub>x</sub> emissions, while panels (e) and (f) show those based on the ODIAC inventory.

448

449 **3.2.2. Comparison of NO<sub>x</sub> and ODIAC Modeled fXCO<sub>2</sub> in Beijing**



450

451 Figure 7 Similar to Fig. 5, comparison between simulated and observed fXCO<sub>2</sub> enhancements using DQ-1 overpasses above Beijing on 9  
452 August 2022 at 18:00 UTC (panels a, c, e) and 16 August 2022 at 18:00 UTC (panels b, d, f). Panels (c) and (d) show the simulated fXCO<sub>2</sub>  
453 enhancements based on the NO<sub>x</sub> emissions, while panels (e) and (f) show those based on the ODIAC inventory.

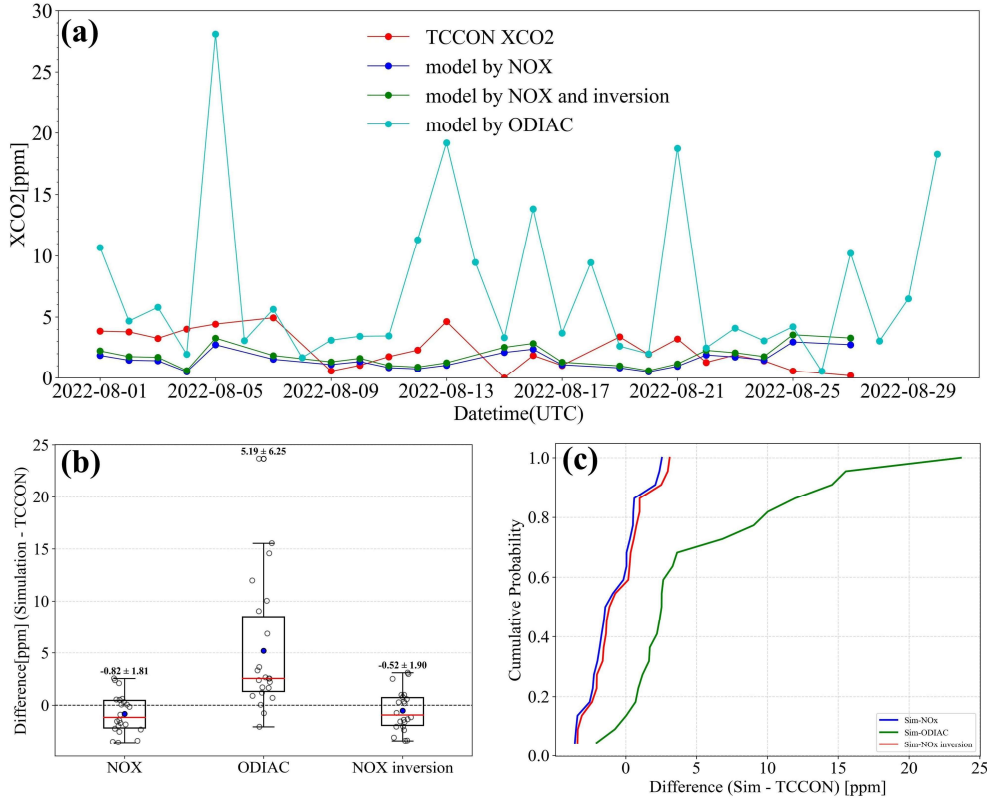
454

455 Figure 7 illustrates the investigation of local fXCO<sub>2</sub> enhancements over Beijing using two DQ-1 overpasses and corresponding  
456 simulated fXCO<sub>2</sub>. In the figure, the colored shading represents XCO<sub>2</sub> concentrations accumulated over the previous 24 hours  
457 simulated by STILT, while the colored dots indicate satellite-observed XCO<sub>2</sub> enhancements, calculated by subtracting the

458 background values (see Section 2.2.2). The red contours outline the urban area of Beijing. As shown, fXCO<sub>2</sub> over this region can  
459 reach approximately 6.0 ppm.

460 Notably, simulations based on the NO<sub>x</sub> inventory (Figs. 7c, d) show that the spatial distribution of fXCO<sub>2</sub> enhancements varies  
461 significantly with meteorological conditions and emission patterns. In contrast, for Paris and Cairo, the simulated fXCO<sub>2</sub> is more  
462 concentrated. Over Beijing, however, the fXCO<sub>2</sub> distribution is more dispersed and comprises multiple plumes. When comparing  
463 simulations using NO<sub>x</sub> and ODIAC inventories for Paris and Cairo, the overall plume structures remain largely unaffected. Over  
464 Beijing, the simulations using the ODIAC inventory (Figs. 7e, f) display an almost identical fXCO<sub>2</sub> enhancement distribution across  
465 different wind conditions, showing pronounced anomalies in the urban area. Such similarity is unrealistic.

466 We attribute this behavior to the ODIAC inventory allocating disproportionately high fossil fuel emissions to central Beijing.  
467 When STILT footprints intersect the urban area, the high emission gradients in ODIAC (central urban emissions far exceeding  
468 suburban values) amplify fXCO<sub>2</sub> enhancements in the inner city. ODIAC's low-emission thresholds are influenced by nighttime  
469 light saturation, with median differences ranging from 47% to 84%. Consequently, ODIAC artificially concentrates emissions in the  
470 city center while underrepresenting surrounding suburban areas. This makes it challenging to accurately constrain CO<sub>2</sub> fluxes in the  
471 peripheral regions using ODIAC. Observations from the TCCON Xianghe site further highlight the limitations of ODIAC's emission  
472 allocation in the Beijing area.



473  
 474 **Figure 8 Comparison of fXCO<sub>2</sub> observed at the TCCON Xianghe site in Beijing during August with fXCO<sub>2</sub> simulated using the NO<sub>x</sub>**  
 475 **inventory and the ODIAC inventory. Panel (a) shows the fXCO<sub>2</sub> observed by TCCON (red line), simulated fXCO<sub>2</sub> using the NO<sub>x</sub>**  
 476 **emissions (dark blue line), simulated fXCO<sub>2</sub> using the ODIAC inventory (light blue line), and simulated fXCO<sub>2</sub> using the posterior NO<sub>x</sub>**  
 477 **emissions (green line). Panel (b) presents the distribution of differences between simulated fXCO<sub>2</sub> (from the NO<sub>x</sub> and ODIAC inventories)**  
 478 **and TCCON observations throughout August, with bold numbers indicating the mean and standard deviation. Panel (c) shows the**  
 479 **cumulative probability distributions of the differences between simulated fXCO<sub>2</sub> (NO<sub>x</sub> emissions and ODIAC inventory) and TCCON**  
 480 **observations.**

481  
 482 Figure 8 presents the comparison of August fXCO<sub>2</sub> at the TCCON site with simulations using the ODIAC and NO<sub>x</sub> inventories.  
 483 Unlike the fXCO<sub>2</sub> calculation described in Section 2.2.2, the TCCON observations provide daily-averaged fossil fuel CO<sub>2</sub>  
 484 enhancements, where TCCON fXCO<sub>2</sub> is calculated as TCCON XCO<sub>2</sub> minus background XCO<sub>2</sub> and NEE contributions (details in  
 485 the Appendix A3). In Figure 8a, the dark blue line represents fXCO<sub>2</sub> simulated at the TCCON site using the NO<sub>x</sub> inventory, the  
 486 green line shows the fXCO<sub>2</sub> simulated after optimization with the inversion using DQ-1 observations, the light blue line corresponds  
 487 to ODIAC-based simulations, and the red line depicts TCCON-observed fXCO<sub>2</sub>.

488 Figure 8b quantifies the accuracy of the simulations by plotting the difference between the simulated ffXCO<sub>2</sub> and TCCON  
 489 observations on the same day and summarizing the monthly mean and standard deviation. The monthly mean absolute difference  
 490 for the NO<sub>x</sub> inventory is 0.82 ppm, while ODIAC exhibits a much larger discrepancy of 5.19 ppm. The inversion-constrained NO<sub>x</sub>  
 491 inventory reduces the mean absolute difference to 0.52 ppm, closely matching TCCON observations. Figure 8c shows the  
 492 cumulative probability distribution of the differences between simulated and observed ffXCO<sub>2</sub>. The differences for the NO<sub>x</sub> and  
 493 inversion-constrained NO<sub>x</sub> simulations are largely centered around zero (blue and red lines), whereas for ODIAC, approximately  
 494 30% of differences exceed 5 ppm.

495 These results indicate that for Beijing in August, simulations based on the NO<sub>x</sub> inventory outperform those using ODIAC.  
 496 Given that the prior ffCO<sub>2</sub> emissions in both inventories are of similar magnitude, the observed discrepancies are primarily  
 497 attributable to the spatial allocation of emissions in ODIAC. The combined inversion using TROPOMI and ACDL data provides a  
 498 more accurate reconstruction of urban ffXCO<sub>2</sub> plume structures.

### 499 3.2.3. ffCO<sub>2</sub> Inversion Results

500 Table 2 Results of inversion of for CO<sub>2</sub>-to-NO<sub>x</sub> ratio selected cities using DQ-1 XCO<sub>2</sub> data

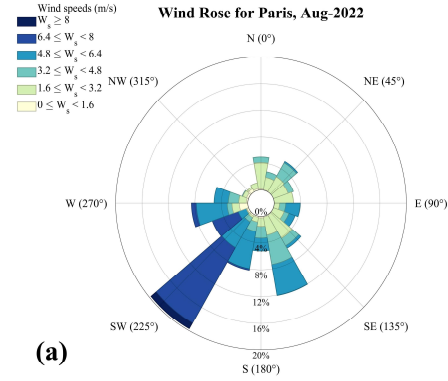
City	Overpass	Prior CO <sub>2</sub> -to- NO <sub>x</sub> ratio ( $\lambda$ )	Prior uncertainty (%)	Observation uncertainty (ppm)	Model transport uncertainty (ppm)	Posterior CO <sub>2</sub> -to-NO <sub>x</sub> ratio ( $\lambda$ ) and uncertainty <del>(%)</del>
Cairo	2022/08/02	470	40.59%	1.23	1.75	428±64.58
	2022/08/19			1.06	2.10	512±96.56
Paris	2022/08/07	601	30.12%	2.45	0.36	731±107.60
	2022/08/21			1.68	0.76	742±138.53
Beijing	2022/08/09	694	28.12%	2.31	1.28	640±90.11
	2022/08/16			1.79	3.25	553±89.80

501 This section presents the inversion results of urban carbon emissions for Cairo, Paris, and Beijing, based on TROPOMI and  
 502 DQ-1 satellite overpass observations (see Table 2). In the inversion, we systematically accounted for observational errors and  
 503 uncertainties in atmospheric transport to improve the reliability of the emission estimates. From the posterior results, we derived  
 504 city-specific CO<sub>2</sub>-to-NO<sub>x</sub> ratios and, by combining them with TROPOMI-derived NO<sub>x</sub> emissions, further quantified fossil fuel CO<sub>2</sub>  
 505 (ffCO<sub>2</sub>) emissions. This approach not only enables quantitative assessment of emissions but also provides a scientific basis for cross-  
 506 city comparisons of emission characteristics, while demonstrating the potential of multi-satellite data for urban emission monitoring.

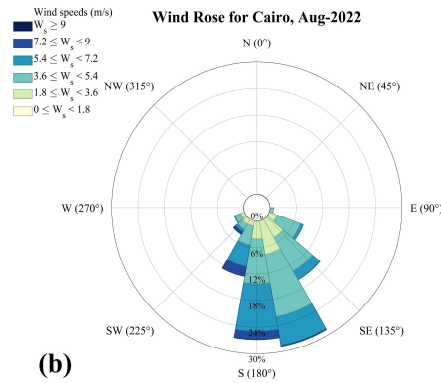
507 For the selected orbits, the posterior CO<sub>2</sub>-to-NO<sub>x</sub> ratios were 428–512 for Cairo, 731–742 for Paris, and 553–640 for Beijing

508 (Table 2). These ratios exhibited clear temporal variability under different background conditions. The magnitude of emissions  
509 captured by each orbit depended strongly on its distance from major emission regions and the contemporaneous domain-averaged  
510 wind conditions(Che et al., 2022). The domain-averaged wind speeds for the study month (Fig. 9), as well as the high-resolution  
511 wind fields at overpass time (black arrows in Figs. 5–7), were consistently greater than  $3 \text{ m s}^{-1}$ . Under such meteorological conditions,  
512 the posterior estimates represent emissions from several hours prior to satellite overpass. The posterior uncertainties of the  $\text{CO}_2$ -to-  
513  $\text{NO}_x$  ratio were 15.09%–18.86% for Cairo, 14.72%–18.67% for Paris, and 14.08%–16.24% for Beijing. Overall, uncertainties were  
514 larger for Cairo and Paris compared with Beijing.

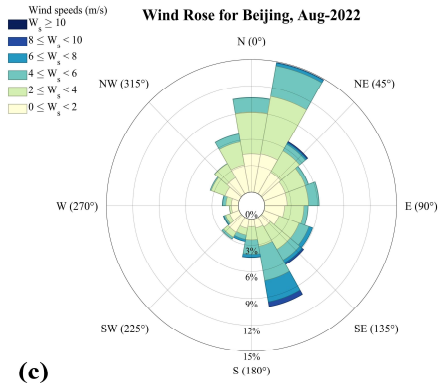
515 As described in section 4.1, the prior uncertainty of the  $\text{CO}_2$ -to- $\text{NO}_x$  ratio was prescribed based on available statistics and  
516 emission characteristics. Owing to more comprehensive statistics and advanced manufacturing processes, large metropolitan areas  
517 typically exhibit better-characterized emission features. Accordingly, the prior uncertainties for Beijing and Paris were smaller than  
518 those for Cairo. Table 2 further shows that the relative contributions of observational and transport errors differed across cities. In  
519 Cairo, transport errors dominated over observational errors, whereas in Paris the opposite held true. For Beijing, the relative  
520 magnitudes of transport and observational errors varied across orbits. The overall smaller posterior uncertainty for Beijing compared  
521 to Cairo and Paris reflects its more stable prior emission characteristics.



(a)



(b)



(c)

Figure 9 Monthly mean wind rose plots for Cairo, Paris, and Beijing in August.

### 3.3. The Uncertainty of Transport Model

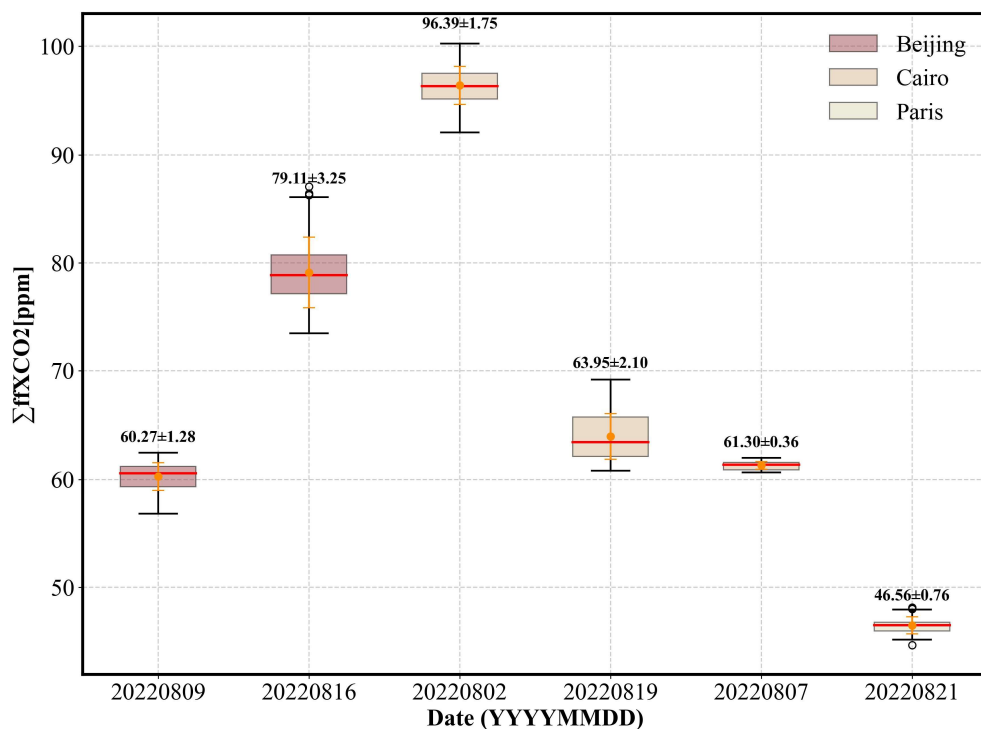
Atmospheric transport modeling uncertainty has been recognized as a major factor affecting emission constraints (Wu et al., 2018). Systematic errors arising from a combination of transport model biases and misrepresented statistical inputs can reduce the magnitude and spatial coverage of terrestrial uncertainty reductions by roughly a factor of two (Wang et al., 2014). Notably, transport-related uncertainties in  $\text{ffXCO}_2$  represent a key source of error in inverse emission estimates (Ye et al., 2020). In this section, we quantify the impact of transport errors on simulated  $\text{XCO}_2$  arising from uncertainties in horizontal wind fields and vertical mixing, with a focus on their influence on the inversion of  $\text{ffXCO}_2$  fluxes.

Errors induced by wind field uncertainties propagate through the model and affect the accuracy of  $\text{CO}_2$  emission estimates (Sheng et al., 2025). Previous studies have accounted for column transport errors by weighting variance relative to pressure and treating each model level independently (Lin and Gerbig, 2005; Wu et al., 2018). Ye et al. 2020 further quantified  $\text{ffXCO}_2$

534 simulation uncertainty by introducing random perturbations in wind speed and direction. Building on these approaches, we  
 535 investigate how horizontal wind speed and wind direction errors influence inversion performance.

536 Here, horizontal transport error is propagated through the model via its effect on fXCO<sub>2</sub> plume dispersion. For the selected  
 537 cities, errors are assumed to be unbiased. Wind direction uncertainty is represented by rotating the plume around the emission center,  
 538 followed by the addition of random wind speed perturbations to the rotated plume. Using DQ-1 wind field data, random errors were  
 539 added at each model level (wind direction perturbation between -10° and 10°, wind speed perturbation between -1 m/s and 1 m/s),  
 540 and the STILT footprints were recomputed to obtain plume-averaged footprints with random errors included (Yi et al., 2024).

541 In total, 10<sup>4</sup> simulations were conducted, with the fXCO<sub>2</sub> integrated along each satellite track. The standard deviation (1σ) of  
 542 these simulations is used to represent the uncertainty in simulated fXCO<sub>2</sub> resulting from horizontal transport errors (Figure 10).



543 Figure 10 Boxplots of modeled integrated fXCO<sub>2</sub> enhancements fXCO<sub>2</sub> along selected DQ-1 overpasses for the three cities (distinguished  
 544 by box color) with dates labeled on the x-axis. For each box, the central line represents the median (q2), and the bottom and top edges  
 545 represent the 25th and 75th percentiles (q1 and q3), respectively. Whiskers extend to the minimum and maximum values. Numbers  
 546 indicate the mean ± standard deviation.  
 547

548  
 549 Figure 10 presents the total simulated fXCO<sub>2</sub> along DQ-1 overpasses for the different study regions. Overall, the simulated

fXCO<sub>2</sub> totals for the three cities are of comparable magnitude. Notably, compared with Beijing and Cairo, the horizontal transport uncertainty along the two Parisian tracks is the lowest, at 0.36 ppm and 0.76 ppm, respectively. In Cairo, the satellite tracks traverse the edges of emission plumes, making the simulations highly sensitive to wind speed and direction, which results in larger transport model errors. Beijing, with its complex terrain and variable wind fields, exhibits more intricate transport uncertainties relative to the other two cities. These observations indicate that transport model uncertainty is closely related to city-scale emissions, the relative alignment of plumes and satellite tracks, model performance, and local topography. Variations in these factors contribute to temporal changes in posterior emission uncertainties along different tracks.

Vertical turbulent mixing governs the vertical transport of air parcels and controls the dilution of surface emissions within the boundary layer (Vertical mixing in atmospheric tracer transport models: error characterization and propagation). Although column-integrated measurements may be less sensitive to the vertical distribution of tracers than in situ observations, errors in planetary boundary layer (PBL) height can still affect column simulations due to wind shear and its interaction with vertical redistribution of tracers (Planetary boundary layer errors in mesoscale inversions of column-integrated CO<sub>2</sub> measurements). It is worth noting that the ACDL instrument includes an aerosol channel capable of providing extinction coefficient profiles and planetary boundary layer height (PBLH) products (Dai et al., 2024). In this study, PBLH data derived from ACDL retrievals are used in the simulations, helping to mitigate errors arising from inaccurate boundary layer height assumptions. Therefore, boundary layer height errors are not considered in the estimation of fXCO<sub>2</sub>.

#### 4. Importance of Satellite Observations for Optimizing the CO<sub>2</sub>-to-NO<sub>x</sub> Ratio

##### 4.1. Variations in CO<sub>2</sub>-to-NO<sub>x</sub> ratio calculation methods

Recently, an increasing number of studies have employed NO<sub>x</sub> emissions to estimate fXCO<sub>2</sub> emissions (Feng et al., 2024; Zheng et al., 2020; Xu et al., 2025; Yang et al., 2023; Berezin et al., 2013; Zhang et al., 2022). In inversion methods based on NO<sub>x</sub> emissions, the choice of the prior CO<sub>2</sub>-to-NO<sub>x</sub> ratio directly affects the emission estimates. Uncertainty in the prior ratio propagates to the estimated fXCO<sub>2</sub> emissions, influencing both their magnitude and spatial distribution. To evaluate this effect, we selected several widely used CO<sub>2</sub>-to-NO<sub>x</sub> ratio calculation methods and systematically assessed their associated uncertainties (results see Appendix A6).

— M.1 Grid-level CO<sub>2</sub>-to-NO<sub>x</sub> ratio derived directly from gridded CO<sub>2</sub> and NO<sub>x</sub> inventories (Feng et al., 2024). Since this study scales emissions to the city level, we further fitted the grid-level ratios to obtain city-integrated CO<sub>2</sub>-to-NO<sub>x</sub> ratios. M.1 calculations were based on the GEMS gridded inventory.

— M.2 CO<sub>2</sub>-to-NO<sub>x</sub> ratios calculated using sectoral emission factors for CO<sub>2</sub> and NO<sub>x</sub> (Zheng et al., 2020). We derived city-scale ratios by aggregating across all sectors. M.2 used the GEMS sectoral inventory.

域代码已更改

~~M.3 CO<sub>2</sub>-to-NO<sub>x</sub> ratios derived from near-real-time satellite observations. Background stable NO<sub>x</sub> plumes were used to constrain CO<sub>2</sub> plumes, and joint fitting of the two concentrations was performed using the cross-sectional flux method (Xu et al., 2025; Reuter et al., 2019). The CO<sub>2</sub>-to-NO<sub>x</sub> ratio was obtained directly from the half-width at half-maximum. Following this approach, we used TROPOMI and OCO-2 observations to calculate city-scale ratios.~~

~~M.4 Same as M.2, but the MEIC sectoral inventory was used for Beijing.~~

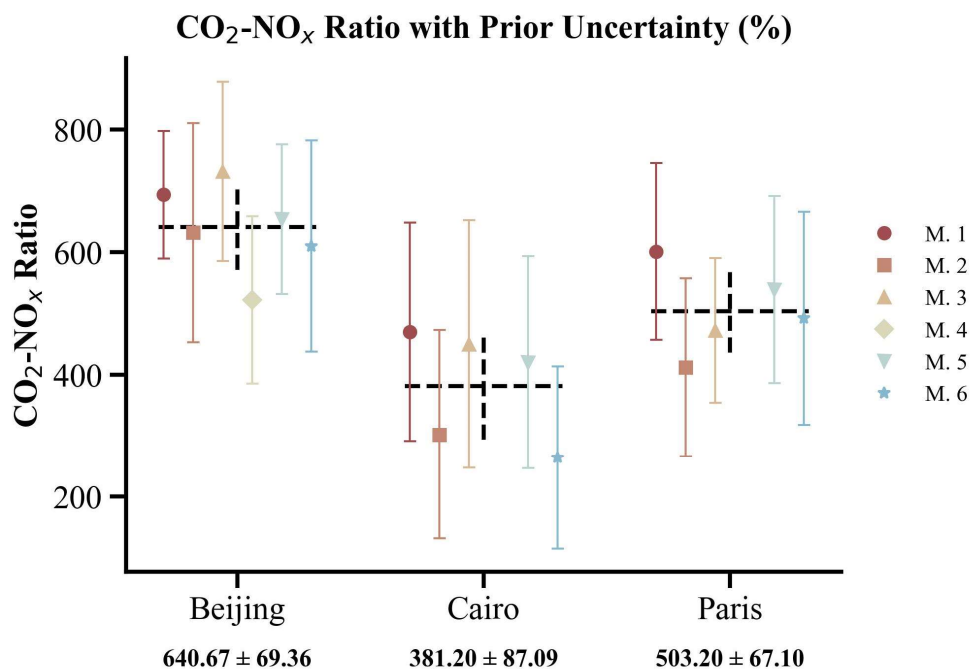
~~M.5 Same as M.1, but calculations were based on the EDGAR gridded inventory.~~

~~M.6 Same as M.2, but calculations were based on the EDGAR sectoral inventory.~~

We systematically accounted for the uncertainties associated with the prior CO<sub>2</sub>-to-NO<sub>x</sub> ratios for each method (see Section 2.2.1 (4) M1-M6). The uncertainty of the CO<sub>2</sub>-to-NO<sub>x</sub> ratio arises from the uncertainties of the underlying emissions. For Method 1, a Monte Carlo simulation was performed: CO<sub>2</sub> and NO<sub>x</sub> inventory uncertainties (Wang et al., 2013; Huang et al., 2017) were used to generate random perturbations at each grid, and the CO<sub>2</sub>-to-NO<sub>x</sub> ratio was recalculated 10,000 times to obtain the distribution characteristics. The prior CO<sub>2</sub>-to-NO<sub>x</sub> ratio uncertainty was expressed as R90/M, where R90 is the range between the 95th and 5th percentiles and M is the median value from 10,000 Monte Carlo simulations. For Method 2, the uncertainty was represented as:

$$\sigma_{C/N} = \sqrt{\sigma_{NO_x}^2 + \sigma_{FFCO_2}^2} \quad (14)$$

where  $\sigma_{NO_x}$  and  $\sigma_{FFCO_2}$  denote the uncertainties of the NO<sub>x</sub> and ffCO<sub>2</sub> emission factors, respectively. Notably, for each method, the use of different inventories requires adjustment of the assigned uncertainties (see Appendix A6). In Method 3, the prior CO<sub>2</sub>-to-NO<sub>x</sub> ratio uncertainty was derived from the quadratic sum of observational uncertainties in NO<sub>2</sub> and CO<sub>2</sub> concentrations and the Gaussian fitting uncertainty.



597

598 **Figure 11** Results of CO<sub>2</sub>-to-NO<sub>x</sub> ratios obtained using different calculation methods for Beijing, Cairo, and Paris. Different CO<sub>2</sub>-to-NO<sub>x</sub>  
 599 ratios within the same city are distinguished by color. Additionally, the mean and standard deviation of the different ratios for each city  
 600 are also shown.

601

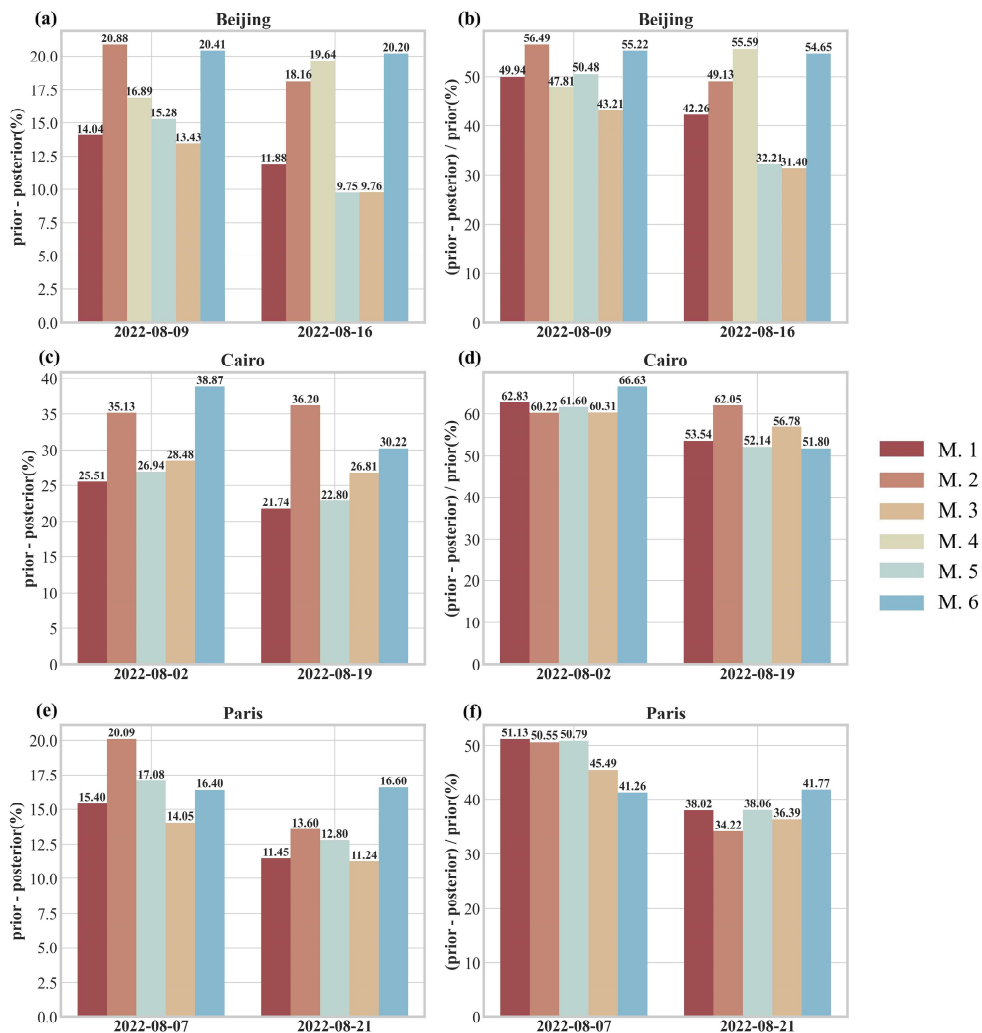
602 In this section, we used six different CO<sub>2</sub>-to-NO<sub>x</sub> ratio calculation methods to estimate the city-scale ratios for Beijing, Cairo,  
 603 and Paris in August. Since the MEIC inventory is only available for Beijing, six prior CO<sub>2</sub>-to-NO<sub>x</sub> ratios were obtained for Beijing,  
 604 while five ratios were derived for Paris and Cairo. Figure 11 presents the CO<sub>2</sub>-to-NO<sub>x</sub> ratios and their associated uncertainties for  
 605 each city using the different methods. We also calculated the mean and standard deviation of the ratios across methods for each city,  
 606 reflecting both the overall understanding of the city-scale prior CO<sub>2</sub>-to-NO<sub>x</sub> ratio and the variability arising from methodological  
 607 differences.

608 The results consistently show the ordering Beijing > Paris > Cairo. Moreover, more developed cities typically have better  
 609 production technologies and more detailed emission statistics(Oda et al., 2019; Ye et al., 2020). Consequently, the prior uncertainties  
 610 for Beijing and Paris are notably smaller than those for Cairo, and the variability of CO<sub>2</sub>-to-NO<sub>x</sub> ratios across methods is also reduced  
 611 for these cities.

612 **4.2. Bayesian Inversion for Reducing CO<sub>2</sub>-to-NO<sub>x</sub> Ratio Uncertainty**

613 Using different prior CO<sub>2</sub>-to-NO<sub>x</sub> ratios, we conducted the Bayesian inversion described in Section 2.2.2 to optimize the August  
614 CO<sub>2</sub>-to-NO<sub>x</sub> ratios for Beijing, Cairo, and Paris along the respective DQ-1 satellite overpasses. Figure 12 shows the absolute  
615 reduction in posterior uncertainty (posterior minus prior) and the relative reduction (prior minus posterior, divided by prior) for each  
616 city across different orbits. For Beijing, the posterior uncertainty decreased by 9.75%–20.88%, corresponding to a 31.4%–56.49%  
617 reduction relative to the prior. In Cairo, the posterior uncertainty decreased by 21.74%–38.87%, equivalent to a 51.8%–66.63%  
618 reduction, while in Paris the reduction ranged from 11.24% to 20.09%, corresponding to a 34.22%–51.13% decrease relative to the  
619 prior.

620 These results indicate that, for all cities, the posterior uncertainties were significantly reduced regardless of the method used to  
621 calculate the prior ratio. This demonstrates that constraining the inversion with DQ-1 ACDL observations substantially improves  
622 the accuracy of fCO<sub>2</sub> estimates derived from NO<sub>x</sub> emissions. Notably, in Cairo—the city with the largest prior uncertainty—the  
623 reduction in uncertainty after constraining with both active and passive satellite observations was the greatest, highlighting the  
624 effectiveness of satellite data in mitigating emission uncertainties in cities with incomplete statistical information. These findings  
625 underscore the potential of satellite remote sensing to supplement emission inventories and enhance the reliability of urban emission  
626 estimates.

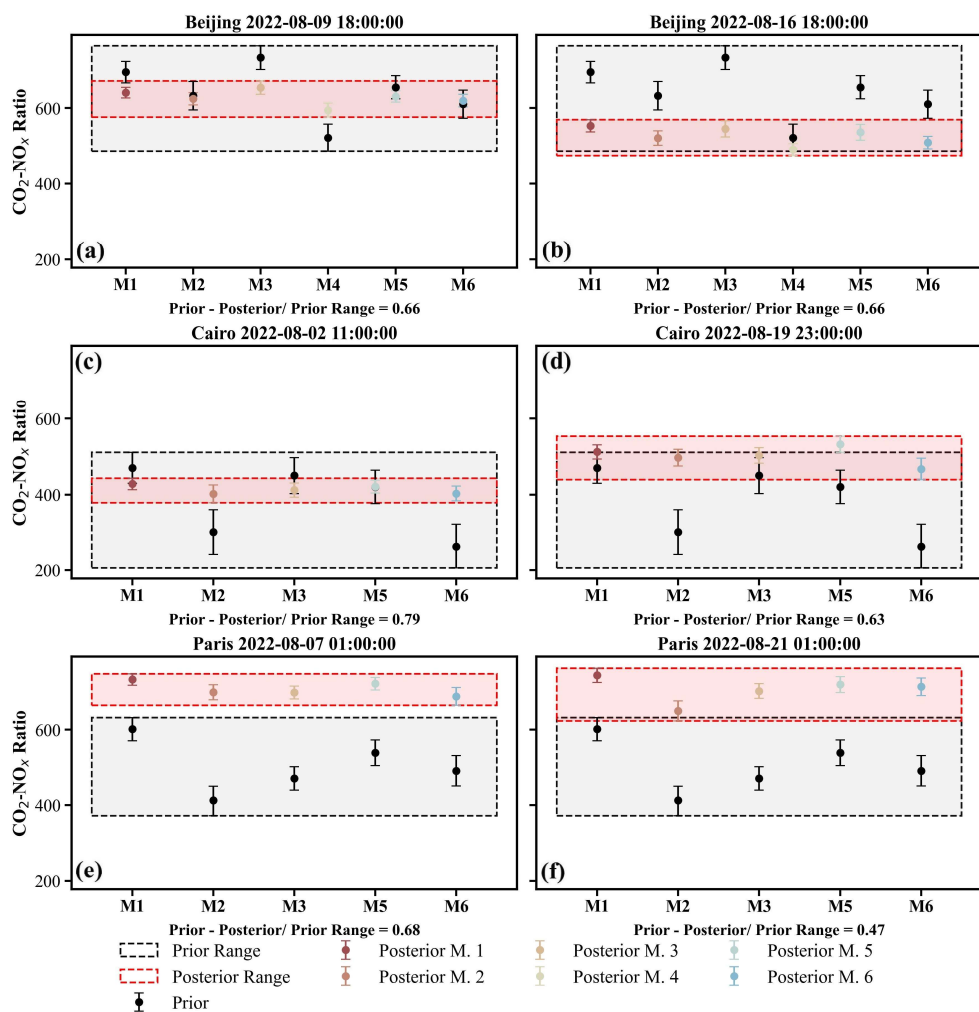


628 **Figure 12 Comparison of Bayesian inversion prior and posterior uncertainties for each orbit over different cities. Panels (a), (c), and (e)**  
 629 **show the absolute reduction in uncertainty (prior uncertainty minus posterior uncertainty), while panels (b), (d), and (f) show the relative**  
 630 **reduction in uncertainty (prior minus posterior uncertainty divided by prior uncertainty). Results from different prior CO<sub>2</sub>-to-NO<sub>x</sub> ratios**  
 631 **are represented by bars in different colors, with the values displayed at the top of each bar.**

632  
 633 Furthermore, we examined the range of CO<sub>2</sub>-to-NO<sub>x</sub> ratios calculated for each city using different methods (Fig. 13). In the  
 634 figure, the black boxes represent the prior distribution ranges, while the red boxes indicate the posterior distribution ranges. The  
 635 distribution ranges illustrate the variability among CO<sub>2</sub>-to-NO<sub>x</sub> ratios obtained from different methods, and we also quantified the

636 reduction of the posterior range relative to the prior. Except for the orbit over Paris on 21 August, all other results show that the  
 637 posterior ranges were reduced by more than 60% compared to the priors.

638 These results demonstrate that our approach effectively reduces the discrepancies arising from different CO<sub>2</sub>-to-NO<sub>x</sub> ratio  
 639 calculation methods. That is, prior ratios derived from various methods are constrained to approximately the same range after  
 640 inversion. This finding underscores the importance of using observational constraints to obtain more accurate CO<sub>2</sub>-to-NO<sub>x</sub> ratios in  
 641 future ffCO<sub>2</sub> emission estimations.



642  
 643 **Figure 13** Distribution ranges of prior and posterior CO<sub>2</sub>-to-NO<sub>x</sub> ratios calculated using different methods. Black boxes represent the  
 644 range of prior CO<sub>2</sub>-to-NO<sub>x</sub> ratios, with posterior ratios indicated by black circles. Red boxes represent the range of posterior CO<sub>2</sub>-to-NO<sub>x</sub>

ratios, with posterior uncertainties from different methods shown using different colors and symbols.

## 5. Summary

Accurate identification and quantification of anthropogenic CO<sub>2</sub> emissions form a critical scientific basis for national emission reduction policies and carbon sink strategies. However, bottom-up inventory approaches typically operate on long compilation cycles (e.g., annual), making it difficult to capture short-term or near-real-time emission dynamics. Most inventories provide only annual totals and lack the temporal resolution needed to characterize daily, hourly, or event-driven emissions.

In this study, we developed a city-scale ffCO<sub>2</sub> inversion framework that integrates both active and passive satellite observations of greenhouse gases. This framework enables high-resolution estimation of fossil fuel emissions at satellite overpass times and over preceding hours, while simultaneously constraining the city-scale CO<sub>2</sub>-to-NO<sub>x</sub> ratio. A key feature of the approach is its reduced reliance on prior emission inventories, allowing rapid and objective identification and quantification of anthropogenic emission signals at regional scales, thereby enhancing the monitoring and verification of urban emission dynamics. In this framework, satellite-observed XCO<sub>2</sub> enhancements attributed to urban emissions are used to constrain WRF-STILT atmospheric transport simulations of anthropogenic CO<sub>2</sub>. This process not only enables quantitative assessment of urban fossil fuel emissions but also provides independent evidence for improving emission inventories and refining urban carbon accounting systems. The study highlights the potential of combining multi-source satellite observations with transport models and lays a foundation for future city-scale ffCO<sub>2</sub> inversions based on the CO<sub>2</sub>-to-NO<sub>x</sub> ratio. Furthermore, we discuss the impact of the lack of standardized CO<sub>2</sub>-to-NO<sub>x</sub> ratio calculation methods on urban emission estimates and demonstrate that observational constraints on city-scale ratios can substantially improve ffCO<sub>2</sub> estimation from a carbon-nitrogen co-optimization perspective. Using a Bayesian inversion approach, we optimized the CO<sub>2</sub>-to-NO<sub>x</sub> ratios for Cairo, Paris, and Beijing in August 2022 based on DQ-1 satellite overpasses and estimated the cities' fossil fuel CO<sub>2</sub> emissions using TROPOMI NO<sub>2</sub> data. The resulting CO<sub>2</sub>-to-NO<sub>x</sub> ratios ranged from 428–512, 731–742, and 553–640 for Cairo, Paris, and Beijing, respectively, indicating significant day-to-day variability in emission estimates. Cairo exhibited the largest posterior uncertainty, primarily due to high prior uncertainty and transport model errors. Differences in posterior uncertainties across orbits were also closely related to meteorological conditions and the relative position of the satellite tracks to urban plumes. We further compared ffXCO<sub>2</sub> enhancement distributions simulated using the ODIAC inventory. Results for Cairo and Paris were broadly consistent with TROPOMI-based simulations, while notable differences emerged for Beijing. TCCON XCO<sub>2</sub> observations were used to interpret these discrepancies. The monthly mean ffXCO<sub>2</sub> enhancement derived from TROPOMI NO<sub>2</sub> data differed from TCCON measurements by less than 1 ppm, whereas the ODIAC-based results deviated by 5.16 ppm. This highlights the need to account for uncertainties arising from inventory allocation and outdated updates when interpreting XCO<sub>2</sub> inversion results. We systematically examined the impact of different prior CO<sub>2</sub>-to-NO<sub>x</sub> ratio calculation methods on urban ffCO<sub>2</sub> inversions. In our study, methodological differences led to variations of 10.8%–22.8% in prior ratios. Importantly, regardless of the prior ratio

675 or its uncertainty, DQ-1 observations constrained the posterior values to a similar range, substantially reducing discrepancies among  
676 different calculation methods.

677 Looking ahead, improving satellite-based city-scale  $\text{ffCO}_2$  inversions will require accounting for the spatiotemporal  
678 correlations of prior emission errors. Our current framework does not yet incorporate this aspect, which imposes certain limitations  
679 on the interpretation and application of the results. Satellite observations are inherently constrained by inversion errors, sampling  
680 geometry, and revisit frequency, limiting overpass opportunities. A single prior factor, such as a uniform  $\text{CO}_2$ -to- $\text{NO}_x$  ratio, cannot  
681 fully capture the complex spatiotemporal features of emissions. Incorporating prior error correlations can mitigate uncertainties  
682 arising from sparse observations and better resolve temporal and spatial variability in urban emissions. Moreover, the number of  
683 satellite tracks required to constrain city emissions depends on the desired emission resolution and uncertainty thresholds relevant  
684 for policy applications. Lower temporal resolution may suffice for long-term trend analysis, whereas capturing short-term peaks or  
685 episodic emissions necessitates higher observation frequency and precision. This consideration aligns with emerging international  
686 approaches emphasizing multi-platform, multi-temporal observations, combining polar-orbiting, geostationary satellites, and  
687 ground-based monitoring to achieve multidimensional constraints on urban emissions.

688 Overall, our results demonstrate that coupling high-resolution atmospheric transport simulations with a Bayesian inversion  
689 framework allows TROPOMI and DQ-1 multi-source observations to effectively constrain urban  $\text{ffXCO}_2$  enhancement signals. The  
690 approach captures spatial heterogeneity of emissions, particularly in cities with strong emission intensities and well-defined plume  
691 structures, providing a robust basis for quantitative analysis. Furthermore, current methods estimating  $\text{ffCO}_2$  from  $\text{NO}_x$  emissions  
692 often lack explicit treatment of  $\text{CO}_2$ -to- $\text{NO}_x$  ratio uncertainty, which can significantly influence inversion outcomes. Differences  
693 among calculation methods for the same region can be as large as 258–304. Notably, our inversion framework substantially reduces  
694  $\text{CO}_2$ -to- $\text{NO}_x$  ratio uncertainty, providing more stable priors for urban  $\text{ffCO}_2$  estimation. Recent studies suggest the need to further  
695 optimize  $\text{CO}_2$ -to- $\text{NO}_x$  emission ratios at regional scales to improve  $\text{ffCO}_2$  estimates (Feng et al., 2024). Therefore, we recommend  
696 that future  $\text{NO}_x$ -based  $\text{ffCO}_2$  inversion studies adopt observational constraints to refine  $\text{CO}_2$ -to- $\text{NO}_x$  ratios, minimizing errors arising  
697 from prior ratio uncertainties.

## 698 **Appendix**

### 699 **A1: ACDL $\text{XCO}_2$ Data Inversion**

700 Unlike passive satellite  $\text{XCO}_2$  products (e.g., OCO-2/3), the DQ-1  $\text{XCO}_2$  product—hereafter referred to as  $\text{XCO}_2^{\text{Lidar}}$  to  
701 distinguish it from passive measurements—is derived from the differential absorption between ACDL’s on-band wavelength (strong  
702  $\text{CO}_2$  absorption) and off-band wavelength (weak  $\text{CO}_2$  absorption). Here, “WF(p)” refers to the lidar signal and integrated weighting  
703 function introduced in Section 2.1.1, with “p” representing atmospheric pressure:

$$XCO_2^{Lidar} = \frac{2 \cdot \ln \left( \frac{V_{off} \cdot V_{on-0}}{V_{on} \cdot V_{off-0}} \right)}{\int_{p_{surface}}^{p_{toa}} WF(p) dp} \quad (A1)$$

Here,  $V_{on}$  and  $V_{off}$  denote the reflected signal energies at the on-band and off-band wavelengths, respectively, while  $V_{on-0}$  and  $V_{off-0}$  correspond to the transmitted signal energies.  $p_{surface}$  represents the atmospheric pressure at the sub-satellite point of the laser, and  $p_{toa}$  denotes the pressure at the top of the atmosphere. The denominator in Equation A1 represents the integrated weighting function ( $WF(p)$ ), which can be expressed according to (Refaat et al., 2016) as:

$$WF(p) = \Delta\sigma_{wf}(\lambda_{on}, \lambda_{off}, p) \cdot N_{dry}(p) \quad (A2)$$

Here,  $\Delta\sigma_{wf}(\lambda_{on}, \lambda_{off}, p)$  represents the differential absorption cross-section of  $CO_2$  between the on-band  $\lambda_{on}$  and off-band  $\lambda_{off}$  wavelengths at pressure  $p$ .  $N_{dry}$  denotes the number of dry air molecules per unit area within the corresponding pressure layer.

**Table A1 DQ-1 ACDL operating parameters**

Parameters	Values
Orbit altitude	705km
Lidar footprint diameter	~70m
Horizontal spacing of lidar footprints	~350m
Field of view	<0.2mrad
Telescope diameter	1000nm
Divergence angle after laser beam expansion	<0.1mrad
Repetition frequency	20Hz
Laser pulse width	<50ns
Laser energy	75mJ
Off-line wavelength	1572.085nm
On-line wavelength	1572.024nm

## A2: Derivation of the Principle of Mass Balance

For satellite column observations of specific species such as  $NO_2$ , the mass balance equation can be expressed as follows:

$$\begin{cases} \frac{\partial V_{NO_2}}{\partial t} + \nabla \cdot \vec{F}_{NO_2} = E_{NO_2} - S \\ \vec{F}_{NO_2} = V_{NO_2} \vec{u}_{100} \\ S \approx \frac{V_{NO_2}}{\tau} \end{cases} \quad (A3)$$

Here,  $V_{NO_2}$  represents the columnar  $NO_2$  concentration observed by TROPOMI, defined as a scalar function of  $x$  and  $\nabla = \left( \frac{\partial}{\partial x}, \frac{\partial}{\partial y} \right)$  denotes the gradient operator;  $\vec{F}_{NO_2} = (F_x, F_y)^T$  is the horizontal flux, with units of  $\text{mol} \cdot \text{m}^{-2} \cdot \text{s}^{-1}$ , expressed as a vector function of  $x$  and  $y$  and weighted by the wind vector. The 100 m wind field is commonly used to characterize horizontal transport within the planetary boundary layer (PBL)(Sun, 2022).  $\tau$  represents the first-order chemical lifetime of  $NO_2$  in seconds.

By solving the system of equations in Equation A3 and expanding the horizontal flux divergence using vector calculus, we obtain the derivation of Equation A4 from Equation A3:

$$\begin{cases} \vec{u}_{100} \cdot (\nabla V_{NO_2}) + V_{NO_2} (\nabla \cdot \vec{u}_{100}) = \nabla \cdot \vec{F}_{NO_2} \\ E_{NO_2} = \frac{\partial V_{NO_2}}{\partial t} + \nabla \cdot \vec{F}_{NO_2} + \frac{V_{NO_2}}{\tau} \end{cases} \quad (A4)$$

Sun et al. 2022, in their first-principles derivation, introduced a "topographic correction term" to replace the wind divergence term  $V_{NO_2} (\nabla \cdot \vec{u}_{100})$ . Beirle et al. 2023 demonstrated that incorporating a topographic correction significantly improves the inversion of power-plant NOx emissions based on the divergence method. Koene et al. 2024 carefully compared these two terms in the derivation of the divergence method, showing that they originate from the continuity equations of the source and non-source terms, and that numerically, the wind divergence and wind-topography terms are approximately equal in the absence of observational errors.

Despite their numerical equivalence in derivation, the accuracy of reanalyzed wind fields is generally lower than that of surface elevation data. Therefore, in practical measurements—particularly in complex, fine-scale settings—the wind divergence term alone may not provide sufficient constraint. Correcting wind divergence artifacts using topographic gradients is more feasible, especially in regions with rugged terrain. Accordingly, we revise Equation A5 using Equation A4 as follows:

$$\frac{V_{NO_2} \vec{u}_{100} \cdot (\nabla z_0)}{H} \approx V_{NO_2} (\nabla \cdot \vec{u}_{100}) \quad (A5)$$

Here,  $\frac{V_{NO_2} \vec{u}_{100} \cdot (\nabla z_0)}{H}$  represents the topographic correction term, where the 10 m wind is approximated as the near-surface wind, and  $H$  denotes the gas scale height in meters. Following previous studies (Beirle et al., 2023; Sun, 2022; Liu et al., 2021), Equation A5 is assimilated over both temporal and spatial dimensions. This procedure is concisely represented using the operator  $(f)$ , as introduced in the derivations by Liu et al. and Sun et al. Ultimately, this approach allows the derivation of the vertical  $NO_2$  flux on a grid-resolved basis.

741 **A3: Atmospheric Model Setting**

742 In this study's application of STILT, hourly outputs from version 4.0 of WRF are used to provide high resolution meteorological  
743 fields, with the model grid configured to 32 vertical (eta) layers. The 6-hourly NCEP FNL (Final) global operational analysis data  
744 ( $ds083.3$ ,  $0.25^\circ \times 0.25^\circ$ ) are used as initial and boundary conditions for meteorological and land surface fields to provide the  
745 initial and boundary conditions for WRF runs. The simulations run for 30 hours, but only the 7th to 30th hours of each simulation  
746 are used to avoid spin-up effects in the first 6 hours.

747 In this study, we used the STILT model, version 2, to simulate atmospheric transport processes. STILT is configured to release  
748 500 particles per receptor each time, with forward dispersion over 24 hours. The particle release heights for STILT are set within  
749 the range of 50-1000 m, with releases every 50 m, and 1000-2000 m, with releases every 100 m, the spatial resolution of the STILT  
750 simulations is  $1 \text{ km} \times 1 \text{ km}$ . Generally, as MAXAGL increases from 1 km to 2 km, the urban enhancement increases and then  
751 stabilizes.

752 **Table A2 Model version information used in this study**

Model	Version
STILT(Stochastic Time-Inverted Lagrangian Transport)	V2
WRF(Weather Research and Forecasting)	V4.0
X-STILT(X-Stochastic Time-Inverted Lagrangian Transport model)	V1

753  
754 **A4: Calculation of NEE XCO<sub>2</sub> enhancement**

755 We performed vertical integration following the method provided by the TCCON team, using the 51 altitude levels listed in  
756 the publicly available `ak_altitude` dataset, which also serve as input heights for the STILT model. In contrast to the XSTILT  
757 calculation method used for DQ-1, we applied the integration operator `integration_operator_x2019` together with the mean averaging  
758 kernel `ak_xco2` to the STILT footprints across the 51 levels in order to generate the simulated XSTILT values required for this study.  
759 We selected the National Institute for Environmental Studies (Japan) data-driven Upscale Product of Global Gross Primary  
760 Production (NEE) as the reference for the overall local NEE during the DQ-1 overpasses. By convolving the NEE inventory with  
761 XSTILT, we simulated the XCO<sub>2</sub> enhancement at TCCON sites attributable to NEE.

762 **A5: Calculation of Priori NO<sub>x</sub> Emission Uncertainty**

763 The uncertainty of the NO<sub>x</sub> inventory derived from the mass balance approach can be estimated using the error propagation  
764 law as follows:

$$\varepsilon_{NOx} = \sqrt{\varepsilon_{\alpha}^2 + \varepsilon_{NO2}^2} \quad (A6)$$

where  $\varepsilon_{\alpha}$  represents the uncertainty in the  $NO_x/NO_2$  ratio, its uncertainty arises from the uncertainties in the input parameters of the chemical model(Liu et al., 2022). And  $\varepsilon_{NO2}$  denotes the uncertainty in the  $NO_2$  flux field. The latter can be further decomposed as:

$$\varepsilon_{NO2} = \sqrt{\varepsilon_{TROPOMI}^2 + \varepsilon_{Wind}^2 + \varepsilon_{Fit}^2} \quad (A7)$$

Here,  $\varepsilon_{TROPOMI}$  is the uncertainty of the  $NO_2$  column concentration,  $\varepsilon_{Wind}$  represents the uncertainty associated with the wind field, and  $\varepsilon_{Fit}$  accounts for the uncertainty in the fitted vertical scale height and chemical lifetime. The uncertainty of  $NO_2$  arises from multiple factors, including spectral fitting, stratospheric correction, AMF, clouds, vertical profiles, and surface albedo(Boersma et al., 2018; Verhoelst et al., 2021; Van Geffen et al., 2022b; Boersma et al., 2004; Martin et al., 2002; Lu et al., 2025)(Boersma et al., 2018; Verhoelst et al., 2021; Van Geffen et al., 2022; Boersma et al., 2004; Martin et al., 2002; Lu et al., 2025). In this study, we use the ratio of the standard deviation to the mean of the column concentration within the study area as a proxy for the TROPOMI observational noise, integrated over the time series. It should be noted that this proxy is calculated based on the oversampled gridded data (also referred to as Level-3) rather than the original Level-2 orbit data. In this study, we do not account for errors introduced during the oversampling of TROPOMI L2 data to the grid(Glissenaar et al., 2025). With appropriate gridding, the uncertainty in polluted areas can be reduced by approximately 20% compared with the original orbits(Sun et al., 2018a)(Sun et al., 2018a). The  $NO_2$  uncertainty is calculated as the ratio of the standard deviation to the mean of the column concentrations within the study region and integrated over the time series. Wind field uncertainty is quantified through  $10^4$  Monte Carlo perturbations of wind speed and direction, with the propagated standard deviation representing the flux variability. The fitting uncertainty is obtained by performing  $10^4$  Monte Carlo draws of the grids involved in the fit, generating ensembles of scale heights and chemical lifetimes, with the final fitting error defined as the root mean square of the standard deviations of these ensembles.

Using the method described above, we quantified the overall uncertainty of  $NO_x$  prior emissions for three cities, as well as the contributions from individual components, with the detailed results summarized in Table A3. It should be noted that the uncertainties reported here represent aggregated values for the entire urban area, rather than detailed uncertainties for individual grid cells.

Based on the uncertainty calculations, the total uncertainty follows the order Beijing (23.79%) > Paris (18.15%) > Cairo (14.31%). A closer look at the contributions of individual components reveals that  $NO_2$  column concentrations and the wind field are the dominant sources, together accounting for more than 66.7% of the total uncertainty. This is attributable to the nature of data-driven dispersion models, in which uncertainties in wind and concentration directly govern the overall uncertainty(Sun, 2022). The nonlinear gradient operations in dispersion models (e.g., second-order difference operators) can amplify white noise in the original concentration field, while in existing emission quantification models, wind fields are considered a major source of uncertainty due to sparse monitoring sites and model errors(Huang et al., 2025).

Among the three cities, NO<sub>2</sub> column inversion uncertainty is highest in Beijing. Unlike Cairo, where high surface reflectivity eases retrievals, Beijing is located in the highly polluted North China Plain with elevated AOD, which increases the difficulty of passive column inversion. In addition, Beijing's complex terrain contributes to the highest wind field uncertainty (~17%) among the three cities. The NO<sub>x</sub>/NO<sub>2</sub> uncertainty is roughly similar across the three cities, consistent with previous studies using NU-WRF (~1.4 ± 0.1). In contrast, the uncertainty associated with first-order chemical lifetime and vertical scale height is the lowest among all components (~1%). This is different from earlier studies (~15%)(Liu et al., 2022) and reflects the benefit of the data-driven fitting approach proposed by Sun et al. (see main text). Since no new assumptions were introduced in the current study, this uncertainty arises solely from the linear fitting model.

**Table A3** The overall uncertainty of NO<sub>x</sub> emissions and the uncertainties of individual components were derived using the dispersion model.

	NO <sub>x</sub> /NO <sub>2</sub> uncertainty(%)	NO <sub>2</sub> uncertainty(%)	Wind uncertainty(%)	Fitted uncertainty(%)	Total uncertainty(%)
Beijing	6.51	15.49	16.76	1.67	23.79
Cairo	4.79	11.64	6.76	0.78	14.31
Paris	5.02	13.67	10.76	1.21	18.15

带格式的: 题注, 与下段同页

带格式的: 列表段落, 段落间距段前: 0 磅

带格式的: 列表段落, 缩进: 首行缩进: 0.71 厘米, 段落间距段前: 0 磅

带格式的: 列表段落, 段落间距段前: 0 磅

格式化表格

带格式的: 列表段落, 缩进: 首行缩进: 0.71 厘米, 段落间距段前: 0 磅

带格式的: 两端对齐, 段落间距段前: 0 磅, 行距: 1.5 倍行距, 无孤行控制

带格式的: 列表段落, 缩进: 首行缩进: 0.71 厘米, 段落间距段前: 0 磅

带格式的: 两端对齐, 段落间距段前: 0 磅, 行距: 1.5 倍行距, 无孤行控制

带格式的: 列表段落, 缩进: 首行缩进: 0.71 厘米, 段落间距段前: 0 磅

带格式的: 两端对齐, 段落间距段前: 0 磅, 行距: 1.5 倍行距, 无孤行控制

**A6: Optimization results of the CO<sub>2</sub>-to-NO<sub>x</sub> ratio obtained using different calculation methods**

**Table A43** Inversion results of CO<sub>2</sub>-to-NO<sub>x</sub> ratios calculated using different methods

Method	City	Date	Prior CO <sub>2</sub> -to-NO <sub>x</sub> ratio (λ)	CO <sub>2</sub> -to-NO <sub>x</sub> ratio uncertainty (%)	NO <sub>x</sub> emission uncertainty (%)	Prior uncertainty (%)	Posterior CO <sub>2</sub> -to-NO <sub>x</sub> ratio (λ)	Posterior uncertainty (%)
1	Beijing	2022/8/9	694	15	23.79	28.12	640	14.08
	Beijing	2022/8/16	694	15	23.79	28.12	553	16.24
	Cairo	2022/8/2	470	37.99	14.31	40.60	428	15.09
	Cairo	2022/8/19	470	37.99	14.31	40.60	512	18.86
	Paris	2022/8/7	601	24.04	18.15	30.12	731	14.72

	Paris	2022/8/21	601	24.04	18.15	30.12	742	18.67
	Beijing	2022/8/9	632	28.28	23.79	36.96	624	16.08
	Beijing	2022/8/16	632	28.28	23.79	36.96	521	18.8
2	Cairo	2022/8/2	302	56.56	14.31	58.34	402	23.21
	Cairo	2022/8/19	302	56.56	14.31	58.34	497	22.14
	Paris	2022/8/7	412	35.35	18.15	39.74	698	19.65
	Paris	2022/8/21	412	35.35	18.15	39.74	649	26.14
	Beijing	2022/8/9	732	20.02	23.79	31.09	653	17.65
	Beijing	2022/8/16	732	20.02	23.79	31.09	545	21.32
3	Cairo	2022/8/2	450	45.81	14.31	47.99	412	18.74
	Cairo	2022/8/19	450	45.08	14.31	47.99	503	20.41
	Paris	2022/8/7	472	24.83	18.15	30.75	697	16.84
	Paris	2022/8/21	472	24.83	18.15	30.75	701	19.65
4	Beijing	2022/8/9	522	26.12	23.79	35.33	594	18.44
	Beijing	2022/8/16	522	26.12	23.79	35.33	491	15.69
	Beijing	2022/8/9	654	18.72	23.79	30.27	630	14.99
	Beijing	2022/8/16	654	18.72	23.79	30.27	536	20.52
5	Cairo	2022/8/2	420	41.32	14.31	43.73	421	16.79
	Cairo	2022/8/19	420	41.32	14.31	43.73	532	20.93
	Paris	2022/8/7	539	28.31	18.15	33.63	720	16.55
	Paris	2022/8/21	539	28.31	18.15	33.63	718	20.83
	Beijing	2022/8/9	610	28.28	23.79	36.96	619	16.55
	Beijing	2022/8/16	610	28.28	23.79	36.96	509	16.76
6	Cairo	2022/8/2	264	56.56	14.31	58.34	403	19.47
	Cairo	2022/8/19	264	56.56	14.31	58.34	467	28.12
	Paris	2022/8/7	492	35.35	18.15	39.74	687	23.34
	Paris	2022/8/21	492	35.35	18.15	39.74	712	23.14

**A7: Posterior fossil fuel emissions distribution for each city**

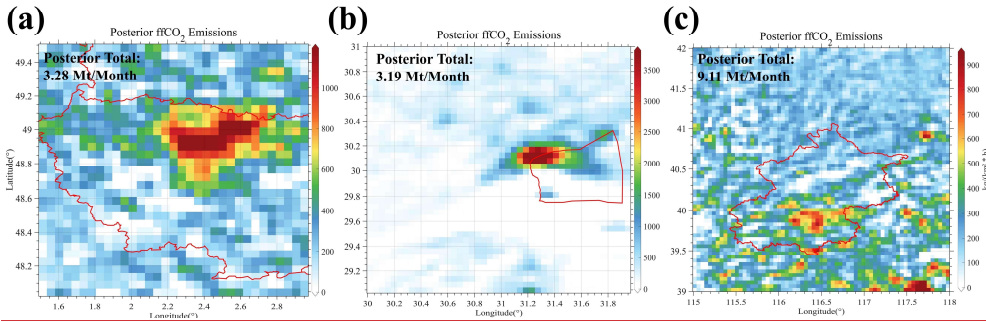


**Figure A1: Posterior fossil fuel carbon dioxide emissions for each city. The red lines outline city boundaries, while the colored shading indicates carbon dioxide emission distribution.**

带格式的: 与下段同页

带格式的: 题注  
设置了格式: 字体: (默认) Times New Roman, (中文) Times New Roman

**Declaration of Competing Interest**

The authors declare that they have no known competing financial interests or personal relationships that could have appeared to influence the work reported in this paper.

**Acknowledgments**

The authors thank all the financial support for this research. This research was supported by the National Key R&D Program of China (Grant No. 2024YFB3910203), National Natural Science Foundation of China(Grant No. 42475144), the Fundamental Research Funds for the Central Universities(2042025kf0036) and Beijing Natural Science Foundation (Grant No. L211045).

**Author contributions**

The experiment design was made by GH and JY. The data collection was done by JY, YH, HL, GH. JY completed the design of the overall WRF-STILT model workflow, data collection, and result analysis. The data analysis was done by HZ, YZ, TS. WG and SL provide funding. The paper was written by JY and GH. All authors have reviewed, commented on, and approved the paper.

**Reference**

Agency, I. E.: World energy outlook, OECD/IEA Paris2009.  
Andres, R. J., Boden, T. A., Bréon, F.-M., Ciais, P., Davis, S., Erickson, D., Gregg, J. S., Jacobson, A., Marland, G., and Miller, J.: A synthesis of carbon dioxide emissions from fossil-fuel combustion, Biogeosciences, 9, 1845-1871, 2012.

带格式的: Reference, 缩进: 左侧: 0 厘米, 悬挂缩进: 4 字符

域代码已更改

827 Ayazpour, Z., Sun, K., Zhang, R., and Shen, H.: Evaluation of the Directional Derivative Approach for Timely and Accurate Satellite-  
828 Based Emission Estimation Using Chemical Transport Model Simulation of Nitrogen Oxides, *Journal of Geophysical Research:*  
829 *Atmospheres*, 130, e2024JD042817, <https://doi.org/10.1029/2024JD042817>, 2025.

830 Beirle, S., Borger, C., Jost, A., and Wagner, T.: Improved catalog of NO<sub>x</sub> point source emissions (version 2), *Earth system science*  
831 *data discussions*, 2023, 1-37, 2023.

832 Berezin, E., Konovalov, I., Ciais, P., Richter, A., Tao, S., Janssens-Maenhout, G., Beekmann, M., and Schulze, E.-D.: Multiannual  
833 changes of CO<sub>2</sub> emissions in China: indirect estimates derived from satellite measurements of tropospheric NO<sub>2</sub> columns,  
834 *Atmospheric Chemistry and Physics*, 13, 9415-9438, 2013.

835 Boersma, K. F., Eskes, H. J., and Brinkma, E. J.: Error analysis for tropospheric NO<sub>2</sub> retrieval from space, *Journal of Geophysical*  
836 *Research: Atmospheres*, 109, <https://doi.org/10.1029/2003JD003962>, 2004.

837 Boersma, K. F., Eskes, H. J., Richter, A., De Smedt, I., Lorente, A., Beirle, S., van Geffen, J. H. G. M., Zara, M., Peters, E., Van  
838 Roozendaal, M., Wagner, T., Maasakkers, J. D., van der A, R. J., Nightingale, J., De Rudder, A., Irie, H., Pinardi, G., Lambert,  
839 J. C., and Compernelle, S. C.: Improving algorithms and uncertainty estimates for satellite NO<sub>2</sub> retrievals: results from the  
840 quality assurance for the essential climate variables (QA4ECV) project, *Atmos. Meas. Tech.*, 11, 6651-6678, 10.5194/amt-11-  
841 6651-2018, 2018.

842 Brenninkmeijer, C. A. and Cai, D. S.: Earth System Chemistry integrated Modelling (ESCiMo) with the Modular Earth Submodel  
843 System (MESSy) version 2.51, *Geoscientific Model Development*, 9, 1153, 2016.

844 Che, K., Lauvaux, T., Taquet, N., Stremme, W., Xu, Y., Alberti, C., Lopez, M., Garcia-Reynoso, A., Ciais, P., and Liu, Y.: CO<sub>2</sub>  
845 emissions estimate from Mexico City using ground-and space-based remote sensing, *Journal of Geophysical Research:*  
846 *Atmospheres*, 129, e2024JD041297, 2024.

847 Che, K., Cai, Z., Liu, Y., Wu, L., Yang, D., Chen, Y., Meng, X., Zhou, M., Wang, J., Yao, L., and Wang, P.: Lagrangian inversion of  
848 anthropogenic CO<sub>2</sub> emissions from Beijing using differential column measurements, *Environmental Research Letters*, 17,  
849 075001, 10.1088/1748-9326/ac7477, 2022.

850 Cheng, C., Liu, D., Wang, S., Zhang, X., Zhang, L., Chen, W., Liu, J., Wan, X., Chen, W., and Chen, X.: Estimating strong point  
851 CO<sub>2</sub> emissions by combining spaceborne IPDA lidar and HSRL, *Remote Sensing of Environment*, 328, 114898, 2025.

852 Crippa, M., Guizzardi, D., Muntean, M., Schaaf, E., Dentener, F., Van Aardenne, J. A., Monni, S., Doering, U., Olivier, J. G., and  
853 Pagliari, V.: Gridded emissions of air pollutants for the period 1970–2012 within EDGAR v4. 3.2, *Earth Syst. Sci. Data*, 10,  
854 1987-2013, 2018.

855 Dai, G., Wu, S., Long, W., Liu, J., Xie, Y., Sun, K., Meng, F., Song, X., Huang, Z., and Chen, W.: Aerosol and cloud data processing  
856 and optical property retrieval algorithms for the spaceborne ACDL/DQ-1, *Atmospheric Measurement Techniques*, 17, 1879-  
857 1890, 2024.

858 Danielson, J. J. and Gesch, D. B.: Global multi-resolution terrain elevation data 2010 (GMTED2010), US Geological Survey2331-  
859 1258, 2011.

860 Dickerson, R. R., Stedman, D. H., and Delany, A. C.: Direct measurements of ozone and nitrogen dioxide photolysis rates in the  
861 troposphere, *Journal of Geophysical Research: Oceans*, 87, 4933-4946, 1982.

862 Eldering, A., Wennberg, P., Crisp, D., Schimel, D., Gunson, M., Chatterjee, A., Liu, J., Schwandner, F., Sun, Y., and O'dell, C.: The  
863 Orbiting Carbon Observatory-2 early science investigations of regional carbon dioxide fluxes, *Science*, 358, eaam5745, 2017.

864 Eskes, H., van Geffen, J., Sneep, M., Veefkind, P., Niemeijer, S., and Zehner, C.: S5P Nitrogen Dioxide v02. 03.01 intermediate  
865 reprocessing on the S5P-PAL system: Readme file, ESA, 12,

866 Feng, S., Jiang, F., Wang, H., Liu, Y., He, W., Wang, H., Shen, Y., Zhang, L., Jia, M., and Ju, W.: China's fossil fuel CO<sub>2</sub> emissions  
867 estimated using surface observations of coemitted NO<sub>2</sub>, *Environmental Science & Technology*, 58, 8299-8312, 2024.

868 Gatley, C. K. and Hutrya, L. R.: Large uncertainties in urban-scale carbon emissions, *Journal of Geophysical Research: Atmospheres*,  
869 122, 11,242-211,260, 2017.

870 Glissenaar, I., Boersma, K. F., Anglou, I., Rijdsijk, P., Verhoelst, T., Compernelle, S., Pinardi, G., Lambert, J.-C., Van Roozendaal,  
871 M., and Eskes, H.: TROPOMI Level 3 tropospheric NO<sub>2</sub> dataset with advanced uncertainty analysis from the ESA CCI+ ECV  
872 precursor project, *Earth System Science Data*, 17, 4627-4650, 2025.

873 Hakkaraian, J., Ialongo, I., and Tamminen, J.: Direct space-based observations of anthropogenic CO<sub>2</sub> emission areas from OCO-  
874 2, *Geophysical Research Letters*, 43, 11,400-411,406, 2016.

875 Han, G., Ma, X., Liang, A., Zhang, T., Zhao, Y., Zhang, M., and Gong, W.: Performance evaluation for China's planned CO<sub>2</sub>-IPDA,  
876 *Remote Sensing*, 9, 768, 2017.

877 Han, G., Xu, H., Gong, W., Liu, J., Du, J., Ma, X., and Liang, A.: Feasibility Study on Measuring Atmospheric CO<sub>2</sub> in Urban Areas  
878 Using Spaceborne CO<sub>2</sub>-IPDA LIDAR, *Remote Sensing*, 10, 985, 2018.

879 Han, G., Huang, Y., Shi, T., Zhang, H., Li, S., Zhang, H., Chen, W., Liu, J., and Gong, W.: Quantifying CO<sub>2</sub> emissions of power  
880 plants with Aerosols and Carbon Dioxide Lidar onboard DQ-1, *Remote Sensing of Environment*, 313, 114368,  
881 <https://doi.org/10.1016/j.rse.2024.114368>, 2024.

882 Han, G., Zhang, H., Huang, Y., Chen, W., Mao, H., Zhang, X., Ma, X., Li, S., Zhang, H., and Liu, J.: First global XCO<sub>2</sub> observations  
883 from spaceborne lidar: methodology and initial result, *Remote Sensing of Environment*, 330, 114954, 2025.

884 Hersbach, H., Bell, B., Berrisford, P., Biavati, G., Horányi, A., Muñoz Sabater, J., Nicolas, J., Peubey, C., Radu, R., and Rozum, I.:  
885 ERA5 hourly data on single levels from 1940 to present, Copernicus climate change service (c3s) climate data store (cds), 10,  
886 2023.

887 Huang, T., Zhu, X., Zhong, Q., Yun, X., Meng, W., Li, B., Ma, J., Zeng, E. Y., and Tao, S.: Spatial and temporal trends in global  
888 emissions of nitrogen oxides from 1960 to 2014, *Environmental science & technology*, 51, 7992-8000, 2017.

889 Huang, Y., Han, G., Shi, T., Li, S., Mao, H., Nie, Y., and Gong, W.: Fi-scape: a divergence theorem based emission quantification  
890 model for air/space-borne imaging spectrometer derived xch<sub>4</sub> observations, *IEEE Journal of Selected Topics in Applied Earth  
891 Observations and Remote Sensing*, 2024.

892 Huang, Y., Han, G., Yi, J., Shi, T., Zhang, Y., Luo, H., Mao, H., Li, S., Mao, F., and Gong, W.: Rapid methane flux estimation  
893 combining MethaneSAT and Sentinel-5P observations: A case study of Turkmenistan, *Geophysical Research Letters*, 52,  
894 e2025GL119369, 2025.

895 Kiemle, C., Ehret, G., Amediek, A., Fix, A., Quatrevalet, M., and Wirth, M.: Potential of Spaceborne Lidar Measurements of Carbon  
896 Dioxide and Methane Emissions from Strong Point Sources, *Remote Sensing*, 9, 1137, 2017.

897 Kiemle, C., Quatrevalet, M., Ehret, G., Amediek, A., Fix, A., and Wirth, M.: Sensitivity studies for a space-based methane lidar  
898 mission, *Atmospheric Measurement Techniques*, 4, 2195-2211, 2011.

899 Koene, E. F. M., Brunner, D., and Kuhlmann, G.: On the theory of the divergence method for quantifying source emissions from  
900 satellite observations, *Journal of Geophysical Research: Atmospheres*, 129, e2023JD039904, 2024.

901 Köhler, P., Guanter, L., Kobayashi, H., Walther, S., and Yang, W.: Assessing the potential of sun-induced fluorescence and the  
902 canopy scattering coefficient to track large-scale vegetation dynamics in Amazon forests, *Remote Sensing of Environment*,  
903 204, 769-785, <https://doi.org/10.1016/j.rse.2017.09.025>, 2018.

904 Kononov, I. B., Berezin, E. V., Ciais, P., Broquet, G., Zhuravlev, R. V., and Janssens-Maenhout, G.: Estimation of fossil-fuel CO  
905 2 emissions using satellite measurements of "proxy" species, *Atmospheric Chemistry and Physics*, 16, 13509-13540, 2016.

906 Le Quéré, C., Andrew, R. M., Friedlingstein, P., Sitch, S., Hauck, J., Pongratz, J., Pickers, P. A., Korsbakken, J. I., Peters, G. P., and  
907 Canadell, J. G.: Global carbon budget 2018, *Earth System Science Data*, 10, 2141-2194, 2018.

908 Lin, J. and Gerbig, C.: Accounting for the effect of transport errors on tracer inversions, *Geophysical Research Letters*, 32, 2005.

909 Liu, F., Tao, Z., Beirle, S., Joiner, J., Yoshida, Y., Smith, S. J., Knowland, K. E., and Wagner, T.: A new method for inferring city  
910 emissions and lifetimes of nitrogen oxides from high-resolution nitrogen dioxide observations: a model study, *Atmospheric  
911 Chemistry and Physics*, 22, 1333-1349, 2022.

912 Liu, F., Duncan, B. N., Krotkov, N. A., Lamsal, L. N., Beirle, S., Griffin, D., McLinden, C. A., Goldberg, D. L., and Lu, Z.: A  
913 methodology to constrain carbon dioxide emissions from coal-fired power plants using satellite observations of co-emitted  
914 nitrogen dioxide, *Atmospheric Chemistry and Physics*, 20, 99-116, 2020.

915 Liu, M., Van Der A, R., Van Weele, M., Eskes, H., Lu, X., Veeffkind, P., De Laat, J., Kong, H., Wang, J., and Sun, J.: A new divergence  
916 method to quantify methane emissions using observations of Sentinel-5P TROPOMI, *Geophysical Research Letters*, 48,  
917 e2021GL094151, 2021.

918 Lu, L., Cohen, J. B., Qin, K., Tiwari, P., Hu, W., Gao, H., and Zheng, B.: New Perspective on Using Observational Uncertainty to

919 Improve Reliability of NO<sub>x</sub> Emissions Over Northern China, *IEEE Transactions on Geoscience and Remote Sensing*, 63, 1-  
920 15, 10.1109/TGRS.2025.3620116, 2025.

921 Martin, R. V., Chance, K., Jacob, D. J., Kurosu, T. P., Spurr, R. J. D., Bucsele, E., Gleason, J. F., Palmer, P. I., Bey, I., Fiore, A. M.,  
922 Li, Q., Yantosca, R. M., and Koelmeijer, R. B. A.: An improved retrieval of tropospheric nitrogen dioxide from GOME,  
923 *Journal of Geophysical Research: Atmospheres*, 107, ACH 9-1-ACH 9-21, <https://doi.org/10.1029/2001JD001027>, 2002.

924 Miller, J. B., Tans, P. P., and Gloor, M.: Steps for success of OCO-2, *Nature Geoscience*, 7, 691-691, 2014.

925 Oda, T. and Maksyutov, S.: ODIAC Fossil Fuel CO<sub>2</sub> Emissions Dataset (version: ODIAC2020b), Center for Global Environmental  
926 Research, National Institute for Environmental Studies [data set], <https://doi.org/10.17595/20170411.001>, 2015.

927 Oda, T., Bun, R., Kinakh, V., Topylko, P., Halushchak, M., Marland, G., Lauvaux, T., Jonas, M., Maksyutov, S., and Nahorski, Z.:  
928 Errors and uncertainties in a gridded carbon dioxide emissions inventory, *Mitigation and Adaptation Strategies for Global  
929 Change*, 24, 1007-1050, 2019.

930 Qin, K., Lu, L., Liu, J., He, Q., Shi, J., Deng, W., Wang, S., and Cohen, J. B.: Model-free daily inversion of NO<sub>x</sub> emissions using  
931 TROPOMI (MCMFE-NO<sub>x</sub>) and its uncertainty: Declining regulated emissions and growth of new sources, *Remote Sensing  
932 of Environment*, 295, 113720, 2023.

933 Refaat, T. F., Singh, U. N., Yu, J., Petros, M., Remus, R., and Ismail, S.: Double-pulse 2- $\mu$ m integrated path differential absorption  
934 lidar airborne validation for atmospheric carbon dioxide measurement, *Applied Optics*, 55, 4232-4246, 2016.

935 Reuter, M., Buchwitz, M., Schneising, O., Krautwurst, S., O'Dell, C. W., Richter, A., Bovensmann, H., and Burrows, J. P.: Towards  
936 monitoring localized CO<sub>2</sub> emissions from space: co-located regional CO<sub>2</sub> and NO<sub>2</sub> enhancements observed by the OCO-2  
937 and SSP satellites, *Atmospheric Chemistry and Physics*, 19, 9371-9383, 2019.

938 Rey-Pommier, A., Chevallier, F., Ciais, P., Christoudias, T., Kushta, J., Georgiou, G., Violaris, A., Dubart, F., and Sciare, J.: Mapping  
939 NO<sub>x</sub> emissions in Cyprus using TROPOMI observations: evaluation of the flux-divergence scheme using multiple parameter  
940 sets, *Environmental Science and Pollution Research*, 32, 1932-1951, 2025.

941 Schwandner, F. M., Gunson, M. R., Miller, C. E., Carn, S. A., Eldering, A., Krings, T., Verhulst, K. R., Schimel, D. S., Nguyen, H.  
942 M., and Crisp, D.: Spaceborne detection of localized carbon dioxide sources, *Science*, 358, eaam5782, 2017.

943 Sheng, M., Hou, Y., Song, H., Ye, X., Lei, L., Ma, P., and Zeng, Z.-C.: Estimating anthropogenic CO<sub>2</sub> emissions from China's  
944 Yangtze River Delta using OCO-2 observations and WRF-Chem simulations, *Remote Sensing of Environment*, 316, 114515,  
945 2025.

946 Sun, K.: Derivation of emissions from satellite-observed column amounts and its application to TROPOMI NO<sub>2</sub> and CO  
947 observations, *Geophysical Research Letters*, 49, e2022GL101102, 2022.

948 Sun, K., Li, L., Jagini, S., and Li, D.: A Satellite Data-Driven Framework to Rapidly Quantify Air Basin-Scale NO<sub>x</sub> Emission and  
949 Its Application to the Po Valley during the COVID-19 Pandemic, *Atmospheric Chemistry and Physics Discussions*, 2021, 1-  
950 29, 2021.

951 Sun, K., Zhu, L., Cady-Pereira, K., Chan Miller, C., Chance, K., Clarisse, L., Coheur, P.-F., González Abad, G., Huang, G., and Liu,  
952 X.: A physics-based approach to oversample multi-satellite, multispecies observations to a common grid, *Atmospheric  
953 Measurement Techniques*, 11, 6679-6701, 2018a.

954 Sun, Y., Frankenberg, C., Jung, M., Joiner, J., Guanter, L., Köhler, P., and Magney, T.: Overview of Solar-Induced chlorophyll  
955 Fluorescence (SIF) from the Orbiting Carbon Observatory-2: Retrieval, cross-mission comparison, and global monitoring for  
956 GPP, *Remote Sensing of Environment*, 209, 808-823, <https://doi.org/10.1016/j.rse.2018.02.016>, 2018b.

957 Team, M.: The Multi-resolution Emission Inventory Model for Climate and Air Pollution Research, MEIC Model [data set], 2012.

958 van Geffen, J., Eskes, H., Compernelle, S., Pinardi, G., Verhoelst, T., Lambert, J. C., Sneep, M., ter Linden, M., Ludewig, A.,  
959 Boersma, K. F., and Veeffkind, J. P.: Sentinel-5P TROPOMI NO<sub>2</sub> retrieval: impact of version v2.2 improvements and  
960 comparisons with OMI and ground-based data, *Atmos. Meas. Tech.*, 15, 2037-2060, 10.5194/amt-15-2037-2022, 2022.

961 Veeffkind, J. P., Aben, I., McMullan, K., Förster, H., De Vries, J., Otter, G., Claas, J., Eskes, H., De Haan, J., and Kleipool, Q.:  
962 TROPOMI on the ESA Sentinel-5 Precursor: A GMES mission for global observations of the atmospheric composition for  
963 climate, air quality and ozone layer applications, *Remote sensing of environment*, 120, 70-83, 2012.

964 Verhoelst, T., Compernelle, S., Pinardi, G., Lambert, J. C., Eskes, H. J., Eichmann, K. U., Fjæraa, A. M., Granville, J., Niemeijer,

965 S., Cede, A., Tiefengraber, M., Hendrick, F., Pazmiño, A., Bais, A., Bazureau, A., Boersma, K. F., Bognar, K., Dehn, A., Donner,  
966 S., Elokhov, A., Gebetsberger, M., Goutail, F., Grutter de la Mora, M., Gruzdev, A., Gratsea, M., Hansen, G. H., Irie, H., Jepsen,  
967 N., Kanaya, Y., Karagiozidis, D., Kivi, R., Kreher, K., Levelt, P. F., Liu, C., Müller, M., Navarro Comas, M., Piters, A. J. M.,  
968 Pommereau, J. P., Portafaix, T., Prados-Roman, C., Puertedura, O., Querel, R., Remmers, J., Richter, A., Rimmer, J., Rivera  
969 Cárdenas, C., Saavedra de Miguel, L., Sinyakov, V. P., Stremme, W., Strong, K., Van Roozendaal, M., Veeffkind, J. P., Wagner,  
970 T., Wittrock, F., Yela González, M., and Zehner, C.: Ground-based validation of the Copernicus Sentinel-5P TROPOMI NO<sub>2</sub>  
971 measurements with the NDACC ZSL-DOAS, MAX-DOAS and Pandonia global networks, *Atmos. Meas. Tech.*, 14, 481-510,  
972 10.5194/amt-14-481-2021, 2021.

973 Wang, J., Kawa, S., Eluszkiewicz, J., Baker, D., Mountain, M., Henderson, J., Nehr Korn, T., and Zaccheo, T.: A regional CO<sub>2</sub>  
974 observing system simulation experiment for the ASCENDS satellite mission, *Atmospheric Chemistry and Physics*, 14, 12897-  
975 12914, 2014.

976 Wang, R., Tao, S., Ciaï, P., Shen, H., Huang, Y., Chen, H., Shen, G., Wang, B., Li, W., and Zhang, Y.: High-resolution mapping of  
977 combustion processes and implications for CO<sub>2</sub> emissions, *Atmospheric Chemistry and Physics*, 13, 5189-5203, 2013.

978 Wei, C.: Historical trend and drivers of China's CO<sub>2</sub> emissions from 2000 to 2020, *Environment, development and sustainability*,  
979 26, 2225-2244, 2024.

980 Wu, D., Lin, J. C., Fasoli, B., Oda, T., Ye, X., Lauvaux, T., Yang, E. G., and Kort, E. A.: A Lagrangian approach towards extracting  
981 signals of urban CO<sub>2</sub> emissions from satellite observations of atmospheric column CO<sub>2</sub> (XCO<sub>2</sub>): X-Stochastic Time-Inverted  
982 Lagrangian Transport model ("X-STILT v1"), *Geoscientific Model Development*, 11, 4843-4871, 2018.

983 Xu, J., Guan, Y., Oldfield, J., Guan, D., and Shan, Y.: China carbon emission accounts 2020-2021, *Applied Energy*, 360, 122837,  
984 2024.

985 Xu, T., Zhang, C., and Liu, C.: Enhanced quantification of global carbon emitters using collocated OCO-3 CO<sub>2</sub> and NO<sub>2</sub>  
986 observations from twin polar-orbiting satellites, *Geophysical Research Letters*, 52, e2025GL116877, 2025.

987 Yang, E. G., Kort, E. A., Ott, L. E., Oda, T., and Lin, J. C.: Using space-based CO<sub>2</sub> and NO<sub>2</sub> observations to estimate urban CO<sub>2</sub>  
988 emissions, *Journal of Geophysical Research: Atmospheres*, 128, e2022JD037736, 2023.

989 Ye, X., Lauvaux, T., Kort, E. A., Oda, T., Feng, S., Lin, J. C., Yang, E. G., and Wu, D.: Constraining fossil fuel CO<sub>2</sub> emissions from  
990 urban area using OCO-2 observations of total column CO<sub>2</sub>, *Journal of Geophysical Research: Atmospheres*, 125,  
991 e2019JD030528, 2020.

992 Yi, J., Huang, Y., Pei, Z., and Han, G.: Urban area observing system (UAOS) simulation experiment using DQ-1 total column  
993 concentration observations, *EGU sphere*, 2024, 1-40, 2024.

994 Yi, J., Huang, Y., Pei, Z., and Han, G.: Urban Area Observing System (UAOS) simulation experiment using DQ-1 total column  
995 concentration observations, *Atmospheric Chemistry and Physics*, 25, 13687-13710, 2025.

996 Zhang, Q., Boersma, K. F., Zhao, B., Eskes, H., Chen, C., Zheng, H., and Zhang, X.: Quantifying daily NO<sub>x</sub> and CO<sub>2</sub> emissions  
997 from Wuhan using satellite observations from TROPOMI and OCO-2, *Atmospheric Chemistry and Physics Discussions*, 2022,  
998 1-18, 2022.

999 Zhang, Q., Streets, D. G., Carmichael, G. R., He, K., Huo, H., Kannari, A., Klimont, Z., Park, I., Reddy, S., and Fu, J.: Asian  
1000 emissions in 2006 for the NASA INTEX-B mission, *Atmospheric Chemistry and Physics*, 9, 5131-5153, 2009.

1001 Zhang, X., Yang, H., Bu, L., Fan, Z., Xiao, W., Chen, B., Zhang, L., Liu, S., Wang, Z., and Liu, J.: Estimation of diurnal emissions  
1002 of CO<sub>2</sub> from thermal power plants using spaceborne integrated path differential absorption (IPDA) lidar, *Atmospheric  
1003 Chemistry and Physics*, 25, 6725-6740, 2025.

1004 Zheng, B., Geng, G., Ciaï, P., Davis, S. J., Martin, R. V., Meng, J., Wu, N., Chevallier, F., Broquet, G., and Boersma, F.: Satellite-  
1005 based estimates of decline and rebound in China's CO<sub>2</sub> emissions during COVID-19 pandemic, *Science advances*, 6, eabd4998,  
1006 2020.

1007

带格式的: Reference, 首行缩进: 0 字符